






Search for brown dwarfs in IC 1396 with *Subaru* HSC: interpreting the impact of environmental factors on substellar population

Saumya Gupta ¹★, Jessy Jose ¹★, Swagat R. Das ², Zhen Guo ^{3,4,5,6}, Belinda Damian,⁷
Prem Prakash⁸ and Manash R Samal ⁹

¹Department of Physics, Indian Institute of Science Education and Research (IISER) Tirupati, Rami Reddy Nagar, Karakambadi Road, Mangalam (PO), Tirupati 517 507, India

²Departamento de Astronomía, Universidad de Chile, Las Condes, 7591245 Santiago, Chile

³Instituto de Física y Astronomía, Universidad de Valparaíso, ave. Gran Bretaña, 1111, Casilla 5030, Valparaíso, Chile

⁴Núcleo Milenio de Formación Planetaria (NPF), ave. Gran Bretaña, 1111, Casilla 5030, Valparaíso, Chile

⁵Centre for Astrophysics Research, University of Hertfordshire, Hatfield AL10 9AB, UK

⁶Departamento de Física, Universidad Técnica Federico Santa María, Avenida España 1680, Valparaíso, Chile

⁷Department of Physics and Electronics, Christ (Deemed to be University), Bangalore 560029, India

⁸Department of Inter Disciplinary, Indian Institute of Technology Hyderabad, Kandi, Sangareddy, Telangana, India

⁹Astronomy and Astrophysics Division, Physical Research Laboratory (PRL), Navrangpura, Ahmedabad 380 009, Gujarat, India

Accepted 2024 January 31. Received 2024 January 30; in original form 2023 September 18

ABSTRACT

Young stellar clusters are predominantly the hub of star formation and hence, ideal to perform comprehensive studies over the least explored substellar regime. Various unanswered questions like the mass distribution in brown dwarf regime and the effect of diverse cluster environment on brown dwarf formation efficiency still plague the scientific community. The nearby young cluster, IC 1396 with its feedback-driven environment, is ideal to conduct such study. In this paper, we adopt a multiwavelength approach, using deep *Subaru* HSC along with other data sets and machine learning techniques to identify the cluster members complete down to $\sim 0.03 M_{\odot}$ in the central 22 arcmin area of IC 1396. We identify 458 cluster members including 62 brown dwarfs which are used to determine mass distribution in the region. We obtain a star-to-brown dwarf ratio of ~ 6 for a stellar mass range $0.03\text{--}1 M_{\odot}$ in the studied cluster. The brown dwarf fraction is observed to increase across the cluster as radial distance from the central OB-stars increases. This study also compiles 15 young stellar clusters to check the variation of star-to-brown dwarf ratio relative to stellar density and ultraviolet (UV) flux ranging within $4\text{--}2500 \text{ stars pc}^{-2}$ and $0.7\text{--}7.3 G_{\odot}$, respectively. The brown dwarf fraction is observed to increase with stellar density but the results about the influence of incident UV flux are inconclusive within this range. This is the deepest study of IC 1396 as of yet and it will pave the way to understand various aspects of brown dwarfs using spectroscopic observations in future.

Key words: methods: data analysis – techniques: photometric – catalogues – brown dwarfs – Hertzsprung–Russell and colour–magnitude diagrams – stars: pre-main-sequence.

1 INTRODUCTION

Brown dwarfs (BDs), defined as self-gravitating substellar objects with mass ranging between $0.013\text{--}0.08 M_{\odot}$, have cool temperatures insufficient to initiate Hydrogen burning in their cores. Several mechanisms proposed for BD formation include turbulent fragmentation, disc fragmentation, dynamical ejection, and photo-erosion (Whitworth & Zinnecker 2004; Bonnell, Clark & Bate 2008; Stamatellos & Whitworth 2009; Whitworth 2018). These substellar sources have been the focus of several past and recent studies in different young star-forming regions such as ONC, NGC 2244, Lupus, ρ Oph, W3, Taurus, Perseus, Sigma Ori, Serpens, Upper Sco, and IC 348 (Scholz et al. 2012; Mužić et al. 2017; Zapatero Osorio, Béjar & Peña Ramírez

2017; Luhman et al. 2018; Esplin & Luhman 2019; Mužić et al. 2019; Jose et al. 2020; Huston & Luhman 2021; Almendros-Abad et al. 2023; Damian et al. 2023a). In spite of such plethora of studies, the exact dominant BD formation mechanism and the factors which determine the BD population in a region still remain vague. Many BD formation mechanisms suggest that the pre-mature ejection of a self-gravitating object results in the formation of very low-mass objects as they are cut-off from the accretion material supply (Whitworth & Zinnecker 2004; Stamatellos & Whitworth 2009; Chabrier et al. 2014; Whitworth 2018). It is hence, expected that the external factors like turbulence, high-energy UV radiation and stellar density may introduce more dynamical perturbations leading to an early ejection of the collapsing cores and enhance the census of BDs formed in a region. Another interesting yet ambiguous subject to investigate here is the mass distribution in substellar regime. Deep studies of Galactic stellar clusters reaching down to the low mass and BD realm are helpful to constrain the stellar evolutionary models. It is

* E-mail: kcsaumya.gupta@gmail.com (SG); jessyvjose1@gmail.com (JJ)

thus, pivotal to obtain robust statistical samples of BDs in various young stellar clusters (< 10 Myr) with diverse environments to shed more light on the ambiguous issues related to the substellar realm.

The young stellar clusters (< 10 Myr) are not much dynamically evolved (Portegies Zwart, McMillan & Gieles 2010; Longmore et al. 2014; Fujii & Portegies Zwart 2016), hence their current mass distribution is closest to the initial mass function (IMF) of the cluster (Kroupa & Boily 2002; Lim et al. 2015). Such young clusters provide a robust sample of stars spanning a wide range of mass and hence, are the ideal test beds to perform deep comprehensive studies of the stellar and substellar population in the region. However, due to obvious observational constraints and high intrinsic reddening from the cluster, it is difficult to observe the faint low-mass and substellar population ($< 0.5 M_{\odot}$) in distant (> 1 kpc) young Galactic star-forming regions. On the contrary, the nearby young clusters affected by minimal extinction like ONC, ρ Ophiuchi, IC 348, and NGC 1333 ($A_V \sim 2$ mag) provide excellent statistical sample to carry out deeper and wider studies in diverse environments. In addition, although spectroscopy is the widely adopted solution of obtaining the stellar parameters in nearby clusters, it is highly time intensive and restricted to a limited number of sources (Alves de Oliveira et al. 2012; Burgasser et al. 2019; Pearson et al. 2021; Damian et al. 2023b). Hence, multiwavelength photometric studies of such star-forming regions with facilities like Pan-STARRS, *Gaia*, *Subaru* Hyper Suprime-Cam (HSC), Gran Telescopio Canarias (GTC), *Hubble Space Telescope*, Canada–France–Hawaii Telescope / Wide-field InfraRed Camera (CFHT/WIRCam), and United Kingdom Infra-Red Telescope / Wide Field Camera (UKIRT/WFCAM) are useful to detect the very low-mass end of stellar population (Mužić et al. 2012; Allers & Liu 2020; Robberto et al. 2020; Das et al. 2023; Damian et al. 2023b).

It is also crucial to understand the effect of diverse environmental conditions on the population of BDs in a cluster. BD fraction is a useful tool to estimate the statistics of BDs formed in a given star-forming event. Any increase or decrease in the BD formation efficiency across diverse cluster environments due to external factors like ultraviolet (UV) flux and stellar density, would imply an inverse effect on the star-to-BD ratio (Whitworth & Zinnecker 2004; Bonnell et al. 2008; Stamatellos & Whitworth 2009; Vorobyov et al. 2017). The feedback-driven cluster environment may promote the formation of BDs in a region by depleting the supply of accreting material from the fragmented low-mass cores. Recent studies have also explored the impact from the presence of OB stars on the formation of BDs (Mužić et al. 2019; Almendros-Abad et al. 2023) for the regions covered under the Sub-stellar Objects in Nearby Young Clusters survey. In this study, we identify and characterize the BDs in a young star-forming region, IC 1396 (see details below), and then compare the star-to-BD ratio with various star-forming regions. We also compile fifteen young stellar clusters to investigate the behaviour of star-to-BD ratio with varying stellar density and incident far-UV (FUV) flux.

1.1 IC 1396

The young star-forming H II region IC 1396 (see Fig. 1), almost 3° in diameter, is associated with the Cepheus OB2 association (Patel et al. 1998; Getman et al. 2007). At a distance of 900–910 pc (Contreras et al. 2002; Sicilia-Aguilar et al. 2006, 2019; Das et al. 2023), this region is ionized by the central binary system HD 206 267 (Pelayo-Baldarrago et al. 2023, and references therein) and is estimated to have an age ranging between 2–5 Myr (Patel et al. 1998; Sicilia-Aguilar et al. 2005, 2013; Getman et al. 2012). The cluster hosts

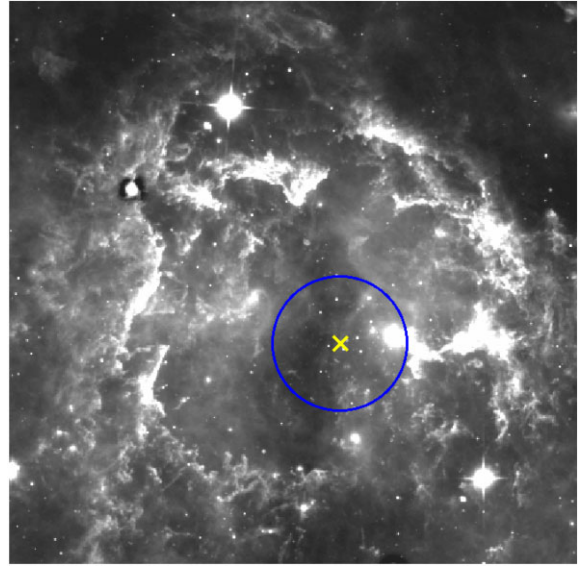


Figure 1. Wide-field Infrared Survey Explorer (WISE) $22 \mu\text{m}$ image of IC 1396 with the circle marking the 22 arcmin radius region studied in this paper. The cross marks the massive star HD 206267.

a prominent cavity at the centre cleared off the dust and gas as a result of ionization from the central massive star. The region is also associated with several bright-rimmed clouds (BRCs), globules, and elephant-trunk structures. The relatively close proximity, minimal uniform extinction ($A_V \sim 1$ – 1.5 mag (Contreras et al. 2002; Sicilia-Aguilar et al. 2005; Sicilia-Aguilar et al. 2013, 2019; Nakano et al. 2012) and ongoing star formation affected by the feedback from massive stars in the region (Sicilia-Aguilar et al. 2004, 2006; Saurin, Bica & Bonatto 2012), make it an ideal target to conduct deep studies regarding low-mass star formation and the factors affecting it.

Several studies have performed the membership classification of the region using techniques like X-ray observations (Mercer et al. 2009; Getman et al. 2012), spectroscopic surveys (Contreras et al. 2002; Sicilia-Aguilar et al. 2006, 2013, 2019; Nakano et al. 2012), $H\alpha$ photometry (Barentsen et al. 2011), and infrared (IR) disc searches (Sicilia-Aguilar et al. 2006; Morales-Calderón et al. 2009; Silverberg et al. 2021). The most recent studies of IC 1396 by Pelayo-Baldarrago et al. (2023) and Das et al. (2023) add extra ~ 500 and 244 new members respectively, to this list using *Gaia* astrometry. In total, all these studies identify 2455 sources as members in the entire 3° diameter region. However, none of these studies are complete for stellar masses $< 0.5 M_{\odot}$ and hence, are inadequate to explore the substellar population in the region. This calls for deeper observations using a wide field-of-view camera on a large telescope which can simultaneously reach down to faint low-mass limits while covering a wider area.

This study aims to perform a BD population analysis within the 22 arcmin region, centred at RA: 324.74° ; Dec.: 57.49° around the massive star HD 206267. The area is specifically chosen for study as more than 60 per cent of the previously identified cluster members as well as disc sources are located within this area. The complex is assumed to have multiple generations of stellar population in BRCs (Sicilia-Aguilar et al. 2006, 2014; Das et al. 2023; Pelayo-Baldarrago et al. 2023) and we focus on the central portion of the cluster.

This work is a premier study to investigate the BD population in IC 1396. It presents a compiled comparative analysis of 15 star-forming regions, which will aid the current colloquy about the role

played by external factors on BD formation efficiency. This paper is organized as follows: Section 2 presents the multiwavelength data sets used for this study. Section 3 discusses the various machine learning (ML) techniques, spectral energy distribution (SED) fitting, and pre-main-sequence (PMS) locus-based identification to obtain a reliable set of members. Consequently, we identify the substellar sources and determine the mass distribution in Section 4. We perform a comparative study of the BD fraction across 15 star-forming regions and discuss its variation relative to stellar density and incident FUV flux in Section 5. A summary of our work along with the future plans are presented in Section 6. Finally, we present the identified BDs in Section 7.

2 DATA SETS USED

The multiwavelength broad-band photometry is a useful approach to detect a substantial sample of substellar objects in nearby young star-forming regions (Alves de Oliveira et al. 2013; Esplin & Luhman 2017; Luhman et al. 2018). However, the multiwavelength photometry approach also requires a reliable member sample which can be used as a template for other sources. The *Gaia* astrometry including proper motion and parallax values for individual sources is ideal to generate such a model member sample. This can be further applied to obtain a deeper set of members using ML techniques. We use optical (*Subaru* HSC, Pan-STARRS DR1, and *Gaia* DR3) in conjunction with near-IR (NIR) (UKIDSS DR11 and 2MASS) data to perform a deep study of the BD realm of the target region.

2.1 Subaru HSC data

We obtained *Subaru* HSC observations for two pointings (central RA: 324.27°; Dec.: 57.91° and RA: 326.37°; Dec.: 57.72°, respectively), each covering an area of 1.5° diameter. The HSC observations were taken on 2017 August 18 (PI: J. Jose; Program ID: S17B0108N), using EAO¹ time in three broad-band optical filters, namely, r_2 , i_2 , and Y (Kawanomoto et al. 2018). The data reduction is conducted following the steps designed in Gupta et al. (2021). The raw data are reduced by HSC pipeline version 6.7 which performs (1) single-visit processing which involves detrending of the raw data, (2) joint calibration which conducts an internal calibration across different visits,² (3) co-addition of various visits to form a single deep image and finally, and (4) co-add processing/multiband analysis which detects individual sources using source extraction and performs photometry on co-added images in the individual filters. For more details on the HSC data reduction please refer Aihara et al. (2018), Bosch et al. (2018), and Gupta et al. (2021).

We obtain a total of 2 401 026 sources detected in either of the three filters (r_2 , i_2 or Y), after data reduction for the entire observed region. However, we will only use the data restricted within the radius of 22 arcmin around the ionizing source HD 206 267 for our analysis due to the aforementioned reasons (see Section 1.1). The photometric results and analysis of a wider area of the complex will be presented in a forthcoming paper (Das et al. (in preparation)). Approximately 254 022 HSC sources are located within the area of interest with photometry in either of the three bands. In order to select sources with good photometry as well as avoid losing genuine sources, we consider only those which have photometric error ≤ 0.1 mag in individual HSC filters (Gupta et al. 2021). The data are

observed to saturate at $r_2 \sim 15.0$ mag corresponding to a source of $\sim 1 M_{\odot}$, and is 90 per cent complete down to 24.5 mag which corresponds to a 0.03–0.035 M_{\odot} source, at a distance of 900 pc, age ~ 2 Myr, and $A_V \sim 1$ mag (Baraffe et al. 2015). We obtain the 90 per cent completeness limit here using the turnover point of source count approach (for details, see Jose et al. 2017; Damian et al. 2021; Gupta et al. 2021). With the help of such deep optical data, we are able to explore well into the substellar realm as discussed in Section 4.

2.2 Pan-STARRS DR1 data

In addition to HSC, we use Pan-STARRS DR1 data³ (Chambers et al. 2016) in r , i , and Y filters to generate the optical catalogue used for our analysis. We consider only those sources for which number of stack detections is > 2 , magnitude in individual bands ≥ 12 mag to avoid source saturation and photometric error in individual filters is ≤ 0.1 mag (Chambers et al. 2016). We use transformation equations given in Gupta et al. (2021) to convert the photometry from Pan-STARRS filter system to HSC system. Pan-STARRS photometry is mainly used here to add sources, especially at the bright end, which are missed in HSC photometry. In total, we have a combined optical catalogue of 258 602 sources which will be further used to identify members in the area of study. We will refer this combined data set as the deep optical catalogue henceforth.

2.3 Gaia DR3 data

We obtained the *Gaia* DR3 data consisting of 48 185 sources from *Gaia* Science archive (*Gaia* Collaboration 2023) in the 22 arcmin radius of IC 1396 and use it to obtain a reliable training set for the identification of members using ML techniques as elaborated in further sections. In order to select genuine *Gaia* sources, we give certain constraints such as parallax > 0 , re-normalized unit weight error (RUWE) < 1.4 , detection in all *Gaia* filters (Lindgren et al. 2021; Pelayo-Baldarrago et al. 2023; Prisinzano et al. 2022) while retrieving the data using Astronomical Data Query Language interface. Since, *Gaia* data are complete between $19 \leq G \leq 20$ mag (*Gaia* Collaboration 2021; Marton et al. 2023), we restrict the sources down to $G \leq 19.5$ mag (average of range 19–20). We thus, obtain 19 432 *Gaia* sources within the 22 arcmin radius of IC 1396.

2.4 UKIDSS GPS DR11/2MASS data

The NIR photometry when used along with deep optical data, gives a broad wavelength range particularly useful for performing SED fitting of the cluster members and obtaining the relevant stellar parameters (Mužić et al. 2019; Damian et al. 2021; Kubiak et al. 2021). We use the deep archived UKIDSS Galactic Plane Survey (GPS) DR11⁴ (Lucas et al. 2008) in J , H , and K bands (Hewett et al. 2006; Lawrence et al. 2007) for this purpose. The UKIDSS GPS DR11 data are retrieved from WFCAM Science archive after applying constraints like $J \geq 13$ mag and photometric errors less than 0.1 mag to only obtain sources with good photometry. In order to include brighter sources, we make use of the 2MASS NIR data (Cutri et al. 2003) downloaded from Vizier in JHK bands with $J < 13$. Also, we select good 2MASS sources based on the quality flags such as $\text{ph_qual} \neq \text{F,E,U}$, $\text{rd_flg} \neq 6$ and $\text{cc_flg} \neq \text{p,d,s,b}$ (Cutri et al.

¹East Asian Observatory.

²Observing shots.

³Downloaded from <https://vizier.u-strasbg.fr/viz-bin/VizieR>

⁴http://wsa.roe.ac.uk/dr11plus_release.html

2003; Guarcello et al. 2021). The concatenated list of sources from 2MASS ($J < 13$ mag) and UKIDSS ($J \geq 13$ mag) forms the deep NIR catalogue of the central 22 arcmin radius region of IC 1396, comprising of 87 614 sources to be used further for our analysis.

3 MEMBERSHIP ANALYSIS

The identification of cluster members based on the stellar proper motion and parallax information is one of the most reliable and widely used methods (Miret-Roig et al. 2019; Olivares et al. 2019; Kubiak et al. 2021; Prisinzano et al. 2022; Das et al. 2023; Pelayo-Baldarrago et al. 2023). Thanks to the consecutive *Gaia* data releases, we now have complete astrometric solutions (proper motion and parallax) available for 1.46 billion stars (Gaia Collaboration 2023). However, the primary drawback here is that it is only complete down to $G \sim 19$ – 20 mag (Gaia Collaboration 2023; Marton et al. 2023; Prisinzano et al. 2022) and hence, quite shallow to identify the faint low-mass cluster members. ML is an extensively used tool which comes to our rescue at this juncture with its unsupervised and supervised techniques like Gaussian Mixture Model (GMM) and Random Forest classifier (RF). Such techniques can accurately classify cluster members and young stellar objects from non-members in young star-forming regions based on the input features (Sarro et al. 2014; Gao 2018b, 2019; Olivares et al. 2019; Melton 2020; Das et al. 2023; Pelayo-Baldarrago et al. 2023).

In this study, we use *Gaia* archived data to form a set of training data by clustering them into members and non-members using the GMM technique. Reliable members and non-members are then utilized in training the RF classifier to identify the probable members among the input deep optical data set. This is followed by SED analysis of the probable members to select confirmed members and deduce their stellar parameters. We briefly describe the procedure adopted to identify members in the area of interest, down to very faint low-mass and substellar sources ($\sim 0.03 M_{\odot}$). Please refer Das et al. (2023) for more details about the procedure followed.

3.1 GMM

GMM is an unsupervised ML technique which categorizes a data set into different clusters based on the probability of each data point associated with a particular group. The technique makes a reasonable assumption that the data set is a collection of normally distributed groups (Sarro et al. 2014; Gao 2018a, b; Cantat-Gaudin et al. 2019; Galli et al. 2020). We initiate our cluster member selection process by generating an efficient training set using *Gaia* DR3 data for the 22 arcmin radius region. However, one of the major limitations of this method is failure to identify clusters due to overcrowding of field stars (Gao 2018a, b; Das et al. 2023). In order to avoid this, we impose few more constraints on astrometric parameters such as proper motion values in the range $-20 \leq \mu_{\alpha} \cos \delta \leq 20$ mas yr $^{-1}$ and $-20 \leq \mu_{\delta} \leq 20$ mas yr $^{-1}$ (Errmann et al. 2013) and distance range within 500–1500 pc (de Zeeuw et al. 1999; Pelayo-Baldarrago et al. 2023) while using the *Gaia* data here. We use the distance estimates from Bailer-Jones et al. (2021). The mentioned constraints on the distance and proper motions are relaxed enough so as not to lose any probable members as well as ensure reduction in the foreground and background contamination in accordance with the values estimated by the previous studies. This aids in generating a robust training data set.

In total, we obtain 2771 *Gaia* sources after applying the above constraints. Among these stars, GMM identifies two groups, namely members and non-members and assigns each star the probability of

being associated to each group. This assignment is based on astrometric parameters, that is, positions, proper motions and parallax information of the star. The sources identified as members and with probability ≥ 0.8 (Gao 2019) are selected for further analysis. The sources identified as non-members by GMM based on their astrometric information, are used as non-member training set further in RF classifier. Since IC 1396 is a young cluster with age < 10 Myr (Sicilia-Aguilar et al. 2005; Das et al. 2023), we further refine the *Gaia* member selection by considering only those sources which are located to the right of the 10 Myr isochrone, corrected for a distance ~ 900 pc and $A_V \sim 1$ mag (Baraffe et al. 2015) in all the colour–magnitude combinations [($G - RP$) versus G , ($BP - RP$) versus BP , ($BP - G$) versus BP]. We present the pmra versus pmdec plots, $BP - RP$ versus BP and $r_2 - Y$ versus r_2 colour–magnitude diagram (CMD) in Figs 2 and 3 for the identified *Gaia*-based members. We eventually secure 411 *Gaia* members which form an ideal training set for RF classifier.

3.2 Random Forest classifier

RF classifier is a widely used supervised learning technique (Galli et al. 2020; Mužić et al. 2022; Das et al. 2023) which performs classification of a new data set based on the training data by using the majority voting approach. The algorithm builds individual decision trees which generate output for each of the different sample subsets of the data. The eventual output of the classification is considered based on the results of the majority of the subsets (Pedregosa et al. 2011). Due to this approach, RF classifier is immune to dimensionality of the feature⁵ space. We identify probable members among the deep optical data by executing RF classifier in three phases. We use the above identified *Gaia* members and non-members with HSC counterparts (see Section 3.1) as the training data set. In the first phase, RF classifier is applied to the 34 859 HSC sources with *Gaia* DR3 counterparts devoid of any constraints applied to it. In this phase, we are able to use *Gaia* parallax and proper motions along with the optical colours [($r_2 - i_2$) versus r_2 ; ($r_2 - Y$) versus r_2] and magnitude ratios (Y/r_2 ; i_2/r_2) of stars as input training features. The RF model, thus trained on the basis of training features mentioned above identifies 792 probable members.

In the second phase, we use this obtained member and non-member set as the training sample for the remaining HSC sources without *Gaia* counterparts and hence, devoid of any parallax and proper motion information of the sources. The RF classifier in this phase uses the same optical colours and magnitude ratios as mentioned above for the training purpose. Using magnitude ratios along with optical HSC colours as input features aids in improving the quality of segregation between the members and non-members, as evident from the receiver operating characteristic (ROC) curves (shown in Appendix A). The hyperparameters used for RF classifier are also listed in Appendix A. For each run of RF classifier, we evaluate the model using train-test-split with test size equal to 40 per cent of the data set and random state equal to 50. We train our algorithm using fivefold cross-validation (CV) with an average CV score of 0.985 and using ROC as the measure of performance. Although, the member sample retrieved so far still does not serve our purpose of investigating the substellar end of the cluster, it provides a robust training sample required to augment the identification of probable cluster members down to the very low mass end.

We understand that the primary reason for the inability of RF classifier to identify cluster members down to the substellar regime

⁵Input attributes useful in learning distinction between different classes.

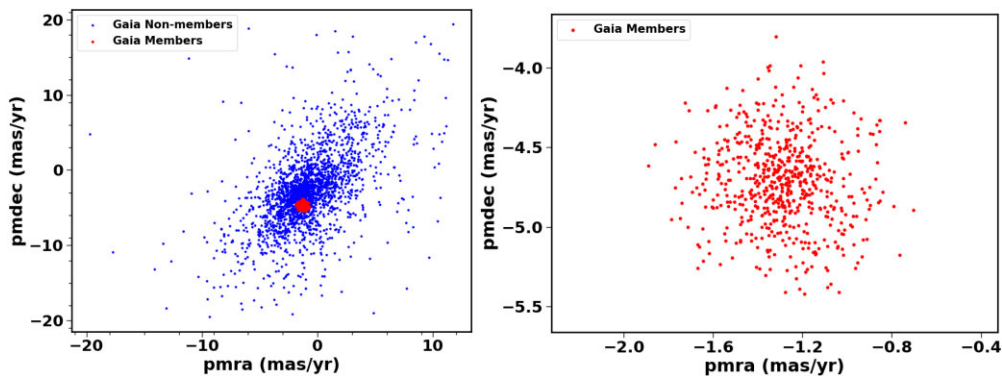


Figure 2. Left: proper motion RA versus proper motion Dec. plot obtained after performing GMM. Right: zoomed version of proper motion RA versus proper motion Dec. plot focused on GMM identified members.

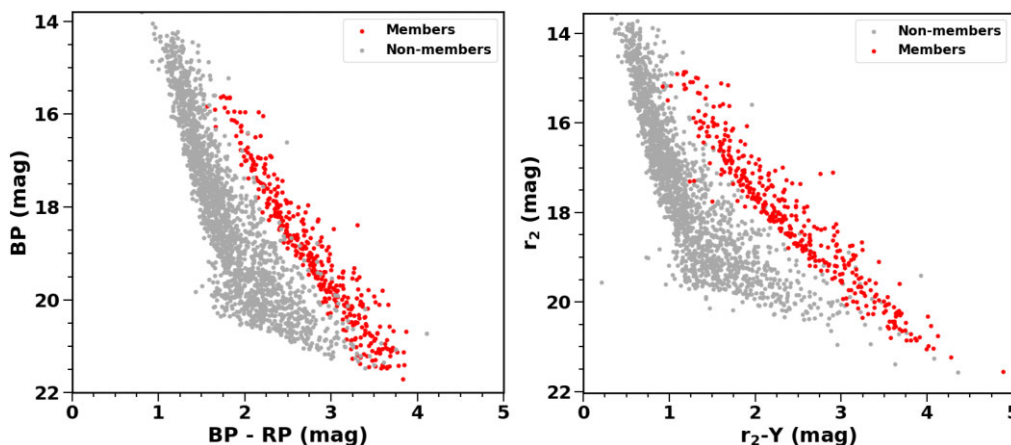


Figure 3. Left: BP – RP versus BP and right: $r_2 - Y$ versus r_2 CMD for members and non-members obtained after performing GMM.

in one run is that the training sample gets biased by the colours of the brighter member stars ($r_2 \leq 19.5$) which forms ~ 50 per cent of the training set. Due to the low signal-to-noise ratio, the scatter in optical colours increases as one approaches the fainter magnitudes. This increase in the deviation in optical colours is considered in fair estimate if we curtail the training and test set to sources with $r_2 > 19.5$ mag for the next phase of RF classifier. The particular threshold of $r_2 > 19.5$ mag is taken because approximately 50 per cent of the probable members procured as of yet, are fainter than this chosen value which, provides a substantial training sample. We hence, use the training set comprising of member and non-member sample ($r_2 > 19.5$ mag) obtained above, and re-apply the RF classifier to the HSC sources with $r_2 > 19.5$ mag. With this approach, the classifier technique predicts probable members down to $r_2 \sim 28$ mag (~ 0.012 – $0.015 M_\odot$ for an age ~ 2 Myr and $A_V \sim 1$ mag), which is well into the substellar regime. We have provided the input features used in all the RF classifier phases along with their relative feature importance in Table 1. The quality parameters attained for each phase are also provided in Table A1 and Fig. A3. In order to be explicit, no probability threshold has been used while selecting probable members during the entire RF classifier method. Another point to note here is that the sources identified as members in all the RF classifier phases are just the probable members. Hence, to remove all the possible contaminants and obtain a clean and accurate list of members along with their stellar parameters like age, mass, etc., we further perform SED fitting of the probable members as described in the following section.

Table 1. Training features used in phases 1, 2, and 3 of RF classifier and their respective importance.

Training feature	Feature importance		
	Phase 1	Phase 2	Phase 3
pmdec	0.25	–	–
Y/r_2	0.21	0.34	0.36
pmra	0.14	–	–
$r_2 - Y$	0.13	0.21	0.20
i_2/r_2	0.12	0.26	0.25
$r_2 - i_2$	0.07	0.20	0.20
Distance	0.07	–	–

3.3 VO SED Analyzer fitting

SED fitting is very useful to estimate the stellar parameters such as age, mass, and effective temperature (T_{eff}) in a star-forming region (Povich et al. 2019; Winston, Hora & Tolls 2020; Olsen et al. 2021). The determination of these parameters helps to understand the evolution of the stellar cluster with respect to age, mass, and environmental factors. In order to obtain a precise estimation of these stellar parameters, a broad wavelength range for the spectral fitting is favourable. Hence, we use UKIDSS DR11/2MASS NIR data along with the deep optical data for this purpose. Among the RF classifier identified probable members, we consider only those 1156 HSC sources, which have counterparts in the deep NIR catalogue.

We use the VO SED Analyzer (VOSA)⁶ tool to build the SEDs using optical to NIR wavelengths (Bayo et al. 2008; Damian et al. 2021; Guzmán-Díaz et al. 2021; Mejías et al. 2022). However as per the requirements of VOSA, we consider only those sources for SED fitting which have photometry in atleast five filters. In addition to the provided photometry, VOSA also uses Pan-STARRS photometry from the online catalogues whenever present using VO services. We also input a distance (900 ± 10 pc) as well as the extinction range ($A_V \sim 1-1.5$ mag) estimates in accordance with the past studies (see references mentioned in Section 1.1), to deredden the SEDs. Subsequently, theoretical models (BT-Settl; Allard, Homeier & Freytag 2012) for solar metallicity are used to obtain the best-fitting model using chi-square minimization. This gives us the physical properties like T_{eff} and luminosity of the stars. The age and mass is derived by fitting the sources in the Hertzsprung–Russell (HR) diagram with BHAC15 isochrones (Baraffe et al. 2015) for a mass range $0.01-1.4 M_{\odot}$ and age ranging between $0.5-10$ Myr. Those sources which do not fulfill these constraints are rejected as contaminants. At this stage, we also remove those sources with *Gaia* DR3 counterparts which do not fulfill the constraints mentioned in Sections 3.1 and 2.3 (e.g. $500 \text{ pc} \leq \text{distance} \leq 1500 \text{ pc}$, $\text{ruwe} < 1.4$, $-20 \leq \mu_{\alpha} \cos \delta \leq 20 \text{ mas yr}^{-1}$, and $-20 \leq \mu_{\delta} \leq 20 \text{ mas yr}^{-1}$). This finally gives us 393 sources as confirmed member sources within the target region of study using ML methods.

We summarize the ML-based approach used to identify the cluster members within the central 22 arcmin radius region here. We first obtain a *Gaia*-based member sample with probability ≥ 0.8 using GMM. This sample is then used as the training set in RF classifier to identify cluster members among the sources with both HSC and *Gaia* photometry. The members identified at this step are further used as training sample for the next phases of RF classifier to segregate members among the HSC sources without *Gaia* counterparts. The members obtained at each step are compiled together and cross-matched with the deep NIR catalogue. SED fitting of these probable members with both optical and NIR photometry is performed using VOSA. We remove sources with *Gaia* counterparts which do not comply with membership constraints. We finally select 393 sources with age < 10 Myr, as cluster members. The identified members however suffer from the restricted sensitivity of UKIDSS (complete down to $\sim 0.09 M_{\odot}$) due to the pre-requisite of having NIR counterparts which is essential for SED fitting. Hence, we adopt an additional approach to identify fainter cluster members by defining a PMS locus as explained below in Section 3.4.

3.4 Additional members from pre-main-sequence locus

It is crucial to extend the member identification to deeper sensitivity independent of NIR counterparts, to perform a comprehensive study of the low-mass population in IC 1396. In order to detect lower mass cluster members ($< 0.09 M_{\odot}$), we define the respective empirical PMS locus for all optical colour–magnitude combinations [$(r_2 - i_2)$ versus r_2 , $(r_2 - Y)$ versus r_2 , and $(i_2 - Y)$ versus i_2] by dividing the magnitude range into 1 mag bins. For each bin, we take mean of the magnitude and median of the colour of sources inside the bin (Damian et al. 2021; Gupta et al. 2021). We then select only those sources which are fainter than $r_2 = 22$ mag and within 1σ (where σ is the standard deviation) limits of the empirical locus defined for the respective colour–magnitude combination. Also, the sources are required to be common in all the colour–magnitude combinations,

which adds to the validation of these sources as cluster members. The particular threshold of $r_2 > 22$ mag is chosen to select the members here as this corresponds to a stellar mass less than $\sim 0.09 M_{\odot}$ (for cluster age and distance). This corresponds to the data completeness of UKIDSS data which restricts the sensitivity of ML-based members obtained in Section 3.3. We obtain 65 members with this approach, thus increasing the total number of cluster members to 458 and detection limit down to $0.03 M_{\odot}$.

Fig. 4 shows $r_2 - i_2$ versus r_2 and $r_2 - Y$ versus r_2 colour–magnitude diagrams overplotted with ML-based, PMS locus-based cluster members, the defined PMS locus and 10 Myr BHAC15 isochrone (Baraffe et al. 2015). The BHAC15 isochrone is corrected for an extinction $A_V \sim 1$ mag and distance ~ 900 pc. We use the Wang & Chen (2019) empirical laws to correct for the extinction. Since BHAC15 isochrones are not available for *Subaru* HSC photometric system, we first convert the available Pan-STARRS 10 Myr isochrone to HSC system using the transformation equations given in Gupta et al. (2021). Subsequently, we correct the 10 Myr isochrone for the distance and reddening of the cluster. In order to determine the mass, these 65 members are first de-reddened for the uniform cluster reddening and age. The mass for each source is then determined using the mass–magnitude relation obtained using BHAC15 models. This member sample is useful to identify BDs and obtain the mass distribution in the region. We would like to mention here that although, reddening across the central 22 arcmin radius region of IC 1396 is uniform with $A_V \sim 1-1.5$ mag, we check if the variation in reddening values may change the output member sample significantly. Hence, we verify the error introduced by varying the A_V upto 1.5 mag and find that a minimal error of ~ 2 per cent is introduced in the statistics of cluster members. Since, the output is approximately uniform, we continue using $A_V = 1$ for our analysis.

In order to verify the validity of member sample obtained by this approach, we perform field subtraction of the central 10 arcmin radius region of IC 1396. For this purpose, we choose a control field of the same area towards the periphery of the region (HSC data for this peripheral region is available by the wide field observations of IC 1396 as mentioned in Section 2). The 10 arcmin radius region is used due to the lack of a larger control field. The statistical field subtraction is then performed, the details of which are provided in Appendix B. The same approach as described above in this section is then used to select members among these statistically field decontaminated sources. We find that the statistics of members and corresponding mass distribution obtained in Section 4.3 remain approximately same whether or not prior field subtraction is performed. This uniformity hence, validates the approach adopted by us above. We therefore, continue with the members obtained above without using field decontamination for further analysis in the paper (detailed supporting reasons are explained in Appendix B).

3.5 Comparison with previous studies

The identified cluster members are high-quality sources with photometric error ≤ 0.1 in optical filters. The proper motions and parallax range of the obtained sources with *Gaia* counterparts (~ 85 per cent) are in excellent accordance with that for literature-based sources (Contreras et al. 2002; Sicilia-Aguilar et al. 2006, 2013; Getman et al. 2007, 2012; Cantat-Gaudin et al. 2018; Das et al. 2023; Pelayo-Baldarrago et al. 2023), as shown in Fig. A2 (top and bottom). The central 22 arcmin radius area of IC 1396 comprises of 857 members ascertained by previous studies such as those mentioned above. An additional ~ 330 members have been identified by the recent *Gaia*-based studies like Cantat-Gaudin et al. (2018), Pelayo-Baldarrago et al. (2023), and Das et al. (2023) within the area of study. Out of

⁶<http://svo2.cab.inta-csic.es/theory/vosa/>

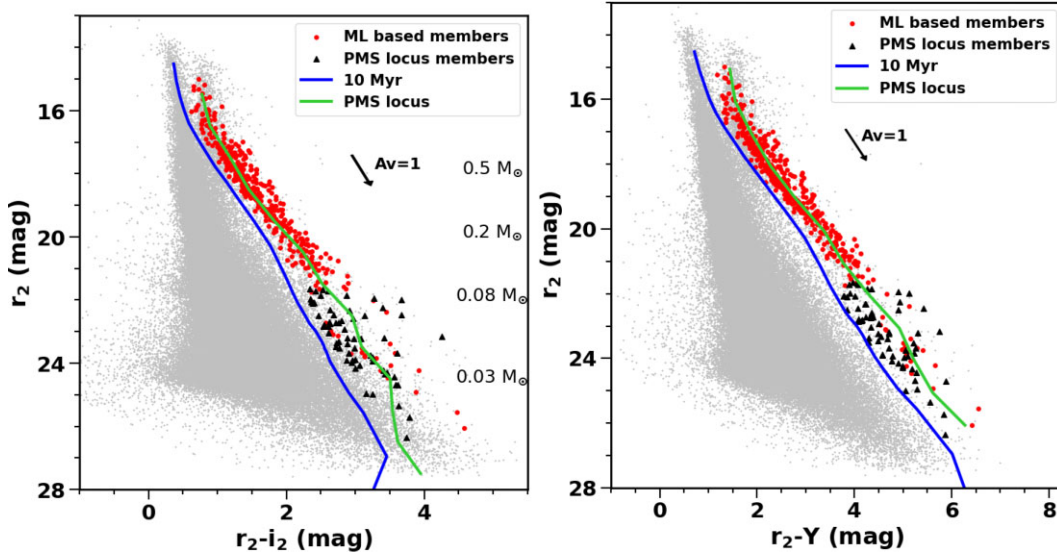


Figure 4. Left: $r_2 - i_2$ versus r_2 colour–magnitude and right: $r_2 - Y$ versus r_2 CMD to obtain members using PMS locus, 10 Myr BHAC15 isochrone and the newly added members.

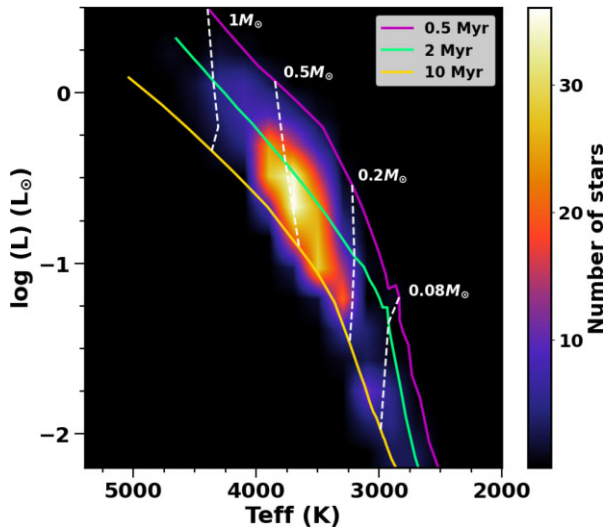


Figure 5. Hess plot of HR diagram of the members obtained from VOSA. BHAC15 isochrones of 0.5, 2, and 10 Myr are overlotted along with mass evolutionary tracks as white dashed curves.

the total 458 member sources confirmed in our study, we retrieve 328 members with counterparts in the literature studies (including both previous studies and recent *Gaia*-based studies mentioned above). The remaining 130 members without counterparts in literature are low mass stars with $r_2 \geq 18$ mag, that is, mass $< 0.5 M_\odot$. This low and substellar mass range is still unexplored for IC 1396 which explains the absence of literature counterparts of these faint sources.

Our study adds 130 new members to the existing cluster member catalogue with detection limit down to ~ 26.5 mag in r_2 band, which corresponds to a $\sim 0.025 M_\odot$ source for the distance and age of the cluster. This significantly enhances the sensitivity down to where IC 1396 can be studied in future. The Hess plot of the HR diagram of members identified in this study is presented in Fig. 5. We use this member list for further analysis in this paper.

4 RESULTS AND ANALYSIS

4.1 Substellar members and their characteristics

We use the obtained members to perform statistical analysis of the region. We determine the substellar population and consequently determine the mass distribution within the studied area. We use the obtained stellar masses of individual member sources in Sections 3.3 and 3.4 to determine if they can be classified as a substellar object. We identify 80 sources with mass $\leq 0.1 M_\odot$ as substellar objects. Out of these, 62 sources have mass $\leq 0.08 M_\odot$, which we classify as BDs. We also derive the age of the member sample using isochrone fitting method. In this method, for each star a weighted average of the age of two nearest isochrones is assigned as the age of the star. We converge this distribution within 2σ limits from the mean age after three iterations (Gupta et al. 2021). We find the median age of the 2σ converged sample to be $\log(\text{Age}) \sim 6.3^{+0.2}_{-0.5}$, which complies with the age of the IC 1396 cluster as estimated in literature (Sicilia-Aguilar et al. 2005; Getman et al. 2012; Nakano et al. 2012; Das et al. 2023).

4.2 Colour–magnitude and colour–colour diagrams

We present here the various CMD and two-colour diagram for the 22 arcmin radius area of study in IC 1396. Both the Hess plots of $(r_2 - Y)$ versus r_2 CMD and $(r_2 - J)$ versus $(J - K)$ two-colour plot [Figs 6 (top left) and (bottom left)] exhibit a distinct PMS branch. The corresponding scatter plots [Figs 6 (top centre, top right, and bottom right)] are overlotted with the identified members and 10 Myr BHAC15 isochrone corrected for the cluster extinction $A_V \sim 1$ mag and distance ~ 900 pc. In these plots, we observe that the identified stellar and substellar members in the region predominantly occupy the distinct PMS branch, which is a typical feature of young star-forming regions (Jose et al. 2017; Damiani et al. 2019; Damiani et al. 2021; Gupta et al. 2021; Ksoll et al. 2021).

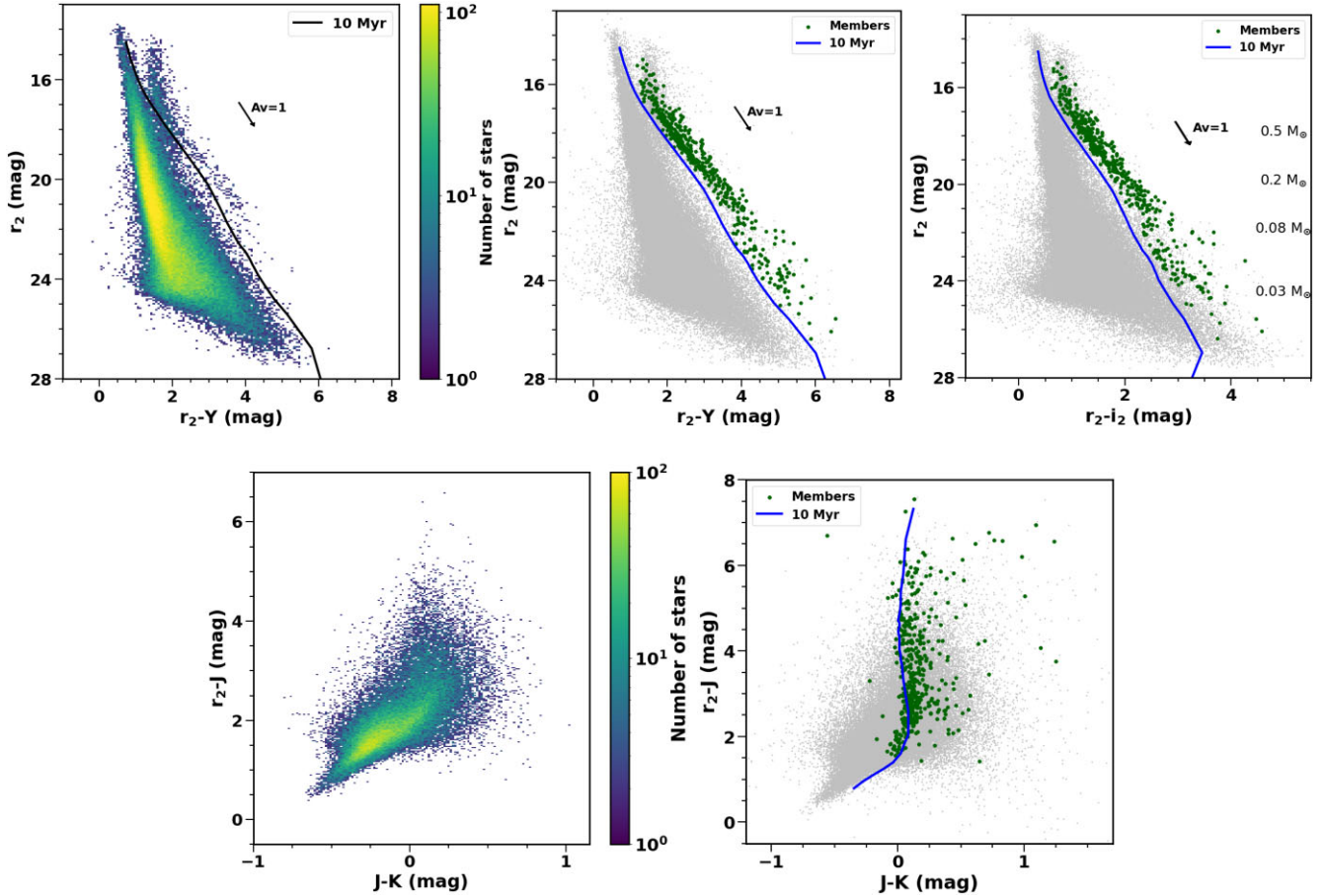


Figure 6. Top left: Hess plot of $(r_2 - Y)$ versus r_2 CMD, top centre: $(r_2 - Y)$ versus r_2 CMD scatter plot, top right: $(r_2 - i_2)$ versus r_2 CMD scatter plot, bottom left: Hess plot of $(r_2 - J)$ versus $(J - K)$ colour–colour plots, and bottom right: $(r_2 - J)$ versus $(J - K)$ scatter colour–colour plots overplotted with 10 Myr BHAC15 isochrone (Baraffe et al. 2015) and identified members.

4.3 Mass distribution

The distribution of stellar mass in a cluster is crucial to understand as well as constrain the star formation process (Kirkpatrick et al. 2012, 2021, 2023; Offner et al. 2014). The obtained member population provides a fair sample of low-mass sources to investigate the nature of mass distribution towards the substellar end. It is also helpful to check the role played by the feedback regulated cluster environment of IC 1396 on the mass apportionment in the region. Due to data completeness issues, we consider the members within the mass range $0.03\text{--}1 M_\odot$ for our analysis. The distribution of stellar mass among the cluster members is estimated by dividing the entire logarithmic mass range into bins of size, $\log M = 0.15$ and the corresponding number of sources in each bin is calculated. The corresponding histogram is shown in Fig. 7. The Poisson error in the count of sources is represented by the error bars in each mass bin of the histogram. We observe a bimodal nature of mass distribution with a secondary peak at $\sim 0.06 M_\odot$ ($\log(M/M_\odot) \sim -1.2$) as the distribution advances in substellar regime. We also observe a sharp dip in the distribution at $\sim 0.10\text{--}0.15 M_\odot$. The bimodal nature of the mass distribution with a secondary peak at $\sim 0.06\text{--}0.1 M_\odot$ and the pronounced dip at the stellar–substellar boundary agrees well with that observed for ONC by Drass et al. (2016). The authors observed a similar bimodal nature of IMF in the feedback-driven ONC region. This suggests a similar BD formation scenario in both IC 1396 and ONC with similar feedback affected cluster environments. A similar secondary

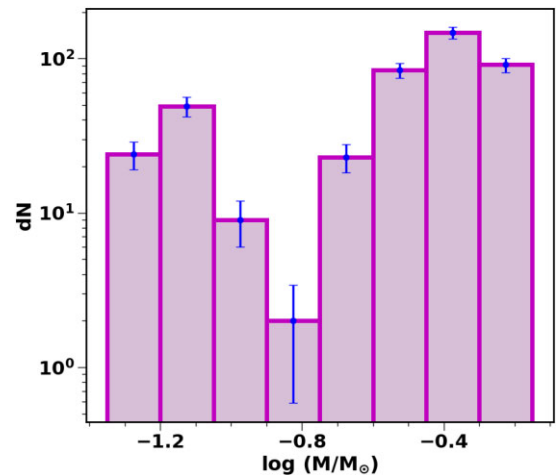


Figure 7. Mass distribution plot for the identified cluster members. The primary peak is $\sim 0.4 M_\odot$. A secondary peak is observed at $\sim 0.06 M_\odot$ and a dip is observed at $\sim 0.1\text{--}0.15 M_\odot$. The error bars represent the Poisson error in the count of sources in each mass bin.

peak has been observed in NGC 2024 by Levine et al. (2006) and Trapezium cluster by Slesnick, Hillenbrand & Carpenter (2004) at $\sim 0.03\text{--}0.05 M_\odot$. However, uncertainties in the derived age of sources affects the mass–luminosity relation, which may influence shape

of mass distribution. The current study pioneers to explore mass distribution down to the so far unexplored substellar realm in the central 22 arcmin radius region of IC 1396.

4.4 Star-to-brown-dwarf ratio

Another useful quantity which gives a fair estimate of the abundance of BDs in a region is the star-to-BD ratio, R . A high R -value indicates lower BD fraction in a stellar cluster. The ratio thus implies the BD formation efficiency in a cluster. An objective comparison of the ratio across varying star-forming environments is important to understand if the BD formation is impacted by the external factors (Mužić et al. 2015, 2017, 2019; Huston & Luhman 2021; Almendros-Abad et al. 2023; Damian et al. 2023b). We consider BDs only within 0.03–0.08 M_{\odot} mass range for the R -value calculation, since the completeness of the data is down to 0.03 M_{\odot} . With the count of stars ranging within 0.08–1 M_{\odot} estimated as 391, the star-to-BD ratio in IC 1396 turns out to be $\sim 6.0 \pm 0.8$, that is, ~ 6 stars for each BD in the region. The error in R is calculated as the Poisson error for the ratio. We emphasize that due to the completeness issues mentioned above, the obtained R -value is evaluated for the stellar mass range 0.03–1 M_{\odot} . The upper limit of stellar mass to determine R is taken as 1 M_{\odot} so as to make a fair comparison between IC 1396 and other star-forming regions. We observe that although towards the higher end, the obtained ratio R is compatible with other young star-forming regions within the statistical uncertainties for the mass range 0.03–1 M_{\odot} . For example, the ratio R ranges within 2–6 in literature for several star-forming regions with diverse cluster environments like ρ Oph, IC348, Lupus3, NGC 2264, and NGC 2244 (Mužić et al. 2012, 2015; Scholz et al. 2013; Almendros-Abad et al. 2023; Kirkpatrick et al. 2023; Damian et al. 2023b) as given in Table 2. This implies a similar BD formation process across various star-forming regions in the Galaxy.

In addition, we check the variation of ratio R with increasing radial distance from the central O-star HD 206267, as shown in Fig. 8. This is obtained by dividing the 22 arcmin radius region into annular bins of equal area, here taken to be $50\pi^2$. The star-to-BD ratio is then calculated for each annular bin based on the number of stars and BDs present in it. The error bars at each point represent the Poisson error obtained for the ratio R in each bin. The limited census of BDs account for the high error observed in the ratio R in the inner annular bins towards the centre of the cluster. The ratio R is observed to decrease as one moves radially outwards away from the centre. This implies that more BDs are located towards the outskirts of the studied area of interest compared to its central part where the ionizing system HD 206 267 is located. The obtained R (~ 6) averaged over our area of study is clearly biased by the very low BD fraction (and hence, considerably higher R values) towards the inner radii (< 3 pc, ~ 12 arcmin) of IC 1396. This is likely contributed by the O-stars at the centre of the cluster. As evident from Fig. 8, the ratio R falls to lower values at distances > 3 pc from the centre. The presence of O-stars thus, seems to inhibit the formation of BDs towards the centre of IC 1396. The BD fraction increases as the incident FUV flux from the central massive stars decreases across the region. It is hence evident that the feedback-driven cluster environment of IC 1396 affects the spatial distribution of BDs within the region.

5 DISCUSSION

The cluster environment in which stars are born plays a crucial role in constraining the star formation and regulating the time-scale for related processes like BD formation, disc evolution, and

planet formation. The quantitative effect of environmental factors on these processes is an interesting problem yet to be fully understood. Although many studies (Bastian, Covey & Meyer 2010; Offner et al. 2014; Damian et al. 2021) suggest a uniformity in IMF behaviour in the high-mass end and hence, a similar star formation process across various star-forming regions, but a non-uniform IMF has been claimed in extreme environments like the Galactic centre and least luminous Milky Way satellites (Lu et al. 2013; Gennaro et al. 2018). Similarly, various theoretical studies also suggest an enhancement in the census of substellar objects in the presence of high gas and stellar density or in the vicinity of massive stars (Whitworth & Zinnecker 2004; Bate 2012; Vorobyov & Basu 2013; Stamatellos 2014). However, more observational evidences in different star-forming environments are still required to support results from theoretical simulations. In this section, we interpret our results and compare them with other star-forming regions as well.

We observe from our study that the mass distribution has a secondary peak in the BD regime [$\log(M/M_{\odot}) \leq -1.1$]. Reipurth & Clarke (2001) find that the bimodal IMF may be attributed to the expulsion of low-mass objects from small clusters of protostars or from the fragmentation of circumstellar discs. A secondary peak towards the BD regime may suggest different formation mechanisms for stars and BDs. We discuss further the dependence of BD population on stellar density and UV flux across various star-forming regions.

5.1 Comparison with other star-forming regions

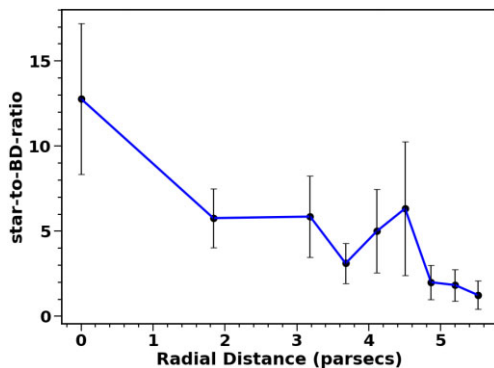
We have compiled a list of 15 star-forming regions with the related information about their ratio R for mass range 0.03–1 M_{\odot} , stellar surface density, and incident FUV flux in Table 2. As evident, the obtained ratio R for IC 1396 is compatible with that estimated for other star-forming regions by different studies. The obtained R value is however, at the higher end of the standard range (2–6) for the star-to-BD ratio. As discussed in Section 4.4, this is due to the steep values of R (> 8) observed towards the inner regions (< 3 pc) of the cluster. The steep R values are attributed to the higher stellar densities observed in the vicinity of central O-stars as compared to the outskirts, which is a result of sequential star formation episodes (Getman et al. 2007; Nakano et al. 2012; Das et al. 2023). Also the FUV flux from O-stars inhibits the BD formation near the cluster centre. Although the ratio R decreases with increasing radial distance from the centre, when averaged over the area of study it tends towards a higher value. The star-to-BD ratio is clearly impacted by the presence of OB-stars ratio across the cluster.

The compiled stellar clusters in Table 2 are well-studied massive Galactic star-forming regions with extreme to low feedback-driven cluster environments. These clusters host a stellar density ranging between ~ 4 –2500 stars pc^{-2} and $\log(\text{flux}_{\text{FUV}}) \sim 0.7$ –7.3 G_{\odot} . We take the mean value of star-to-BD ratios for a cluster if a range of values is calculated in the corresponding reference studies which are listed in the caption of Table 2. In case of different values of the ratio given in multiple reference studies for any region, we adopt the value determined by the most recent available reference study for that cluster. The error bars represent the error in the ratio for each region, either taken directly from the respective reference study or derived by calculating the Poisson error for the ratio. Also, for some regions like NGC 2024 and Westerlund 1 clusters, we have derived the ratio R from their respective mass functions given in the corresponding reference studies since a direct value was not available (see Table 2). For this purpose, we simply calculate number of sources corresponding to the mass function fit performed by the respective authors in the desired mass range (0.03–1 M_{\odot}). The

Table 2. Table shows various star-forming regions with their star-to-BD ratio for mass range $0.03\text{--}1 M_{\odot}$, stellar surface density and dominant FUV flux.

S.no.	Cluster name	Star-to-brown-dwarf ratio	Surface density (pc^{-2})	$\log(\text{flux}_{\text{FUV}})$ (G_0)
1	σ Ori	5.4 ± 1.0	36	4.00
2	IC 348	3.4 ± 0.6	200	2.61
3	NGC 1333	2.1 ± 0.2	185	3.00
4	Chameleon I	4.0 ± 0.5	30	0.90
5	Lupus 3	4.3 ± 0.5	20	0.70
6	ONC	2.4 ± 0.2	350	5.50
7	NGC 2244	2.2 ± 0.3	28	5.74
8	RCW 38	2.0 ± 0.6	2500	6.30
9	ρ Oph	5.1 ± 0.4	79	2.00
10	25 Ori	5.9 ± 0.8	4	4.00
11	NGC 6611	4.4 ± 0.7	138	6.03
12	Westerlund 1	1.5 ± 0.2	295	7.32
13	NGC 2024	3.5 ± 0.4	80	4.80
14	Taurus	4.0 ± 0.6	5	1.30
15	IC 1396	6.0 ± 0.8	15	5.20

References: The reference studies for each region according to their serial number is as follows: (1) B ejar et al. (2011), Pe na Ram rez et al. (2012), Winter & Haworth (2022), Damian et al. (2023b), and references therein; (2) Scholz et al. (2013), Mu zi c et al. (2019), Luhman & Hapich (2020), Damian et al. (2021), and references therein; (3) Scholz et al. (2013), Mu zi c et al. (2019), Knight et al. (2022); (4) and (5) Mu zi c et al. (2015, 2019), Winter (2019); (6) Andersen et al. (2011), Mu zi c et al. (2019), Kim et al. (2022); (7) Mu zi c et al. (2019), Almendros-Abad et al. (2023), and references therein, Damian et al. (2021); (8) Winston et al. (2011), Mu zi c et al. (2017, 2019); (9) Okada et al. (2006), Mu zi c et al. (2012), Miret-Roig et al. (2022); (10) Brice no et al. (2007), Downes et al. (2014), Su arez et al. (2019); (11) Oliveira, Jeffries & van Loon (2009), Damian et al. (2021); (12) Lim et al. (2013), Andersen et al. (2017), Winter & Haworth (2022); (13) Levine et al. (2006), Oliveira et al. (2009), Winter & Haworth (2022); (14) Oliveira et al. (2009), Esplin & Luhman (2019); and (15) Sicilia-Aguilar et al. (2005), Das et al. (2023).

**Figure 8.** Variation of the star-to-BD ratio with respect to distance from the central OB-stars (HD 206267), across the 22 arcmin radius area of study in IC 1396. Each point refers to the star-to-BD ratio in individual annular bin and the corresponding Poisson error represented as error bar.

stellar densities for individual regions were taken directly from the respective reference studies for each region mentioned in the caption of Table 2. The regions for which kernel density estimation plots are available in Mu zi c et al. (2019, e.g. ONC, IC 348, Lupus 3, NGC 1333, RCW 38, NGC 2244, and Cha I), we have considered the stellar density associated with 50 per cent contour. This is consistent with the methods applied in Mu zi c et al. (2019) to compare the R -values among different star-forming regions. In order to find the incident FUV flux in each region we use the respective reference studies and obtain the O-stars catalogue for each region. We then use the results from Guarcello et al. (2016) and Winter & Haworth

(2022) to determine the FUV luminosity and thereby, Habing flux⁷ (G_0) corresponding to the spectral type for O-type stars in individual regions. The FUV fluxes given in Table 2 are the approximate values as we do not add the B-type star fluxes if the region is dominated by O-type stars.

It is important to note here that the larger value of star-to-BD ratio, R in the cluster centre is not an effect of sample bias. This is because IC 1396 is a very sparse cluster and the central crowding does not affect any source detection. However, for crowded star-forming regions (some of them included in Table 2), it may be more difficult to detect BDs in the presence of a concentration of much brighter stars, especially towards the central regions of such clusters. This may have biased the ratio R in such regions towards a higher value.

5.2 Impact of cluster environment

BDs form by the gravitational core-collapse of a molecular core which may get deficient of dust and gas due to its expulsion from the material reservoir (Vorobyov et al. 2017; Riaz, Vanaverbeke & Schleicher 2018). The factors leading to this depletion of material range from photo-erosion due to radiative feedback from nearby massive stars, turbulence to disc instability and subsequent ejection of the low-mass core, thus leaving the formed object in substellar regime (Stamatellos & Whitworth 2009; Chabrier et al. 2014; Whitworth 2018). However, whether the environmental factors play a significant role in deciding the dominant formation mechanism or the census of BDs in a region is yet to be confirmed. Here, we investigate the behaviour of star-to-BD ratio with respect to the two main factors, that is, stellar density and incident FUV flux impacting the cluster environment.

⁷ $G_0 = 1.6 \times 10^{-3} \text{ erg cm}^{-2} \text{ s}^{-1}$.

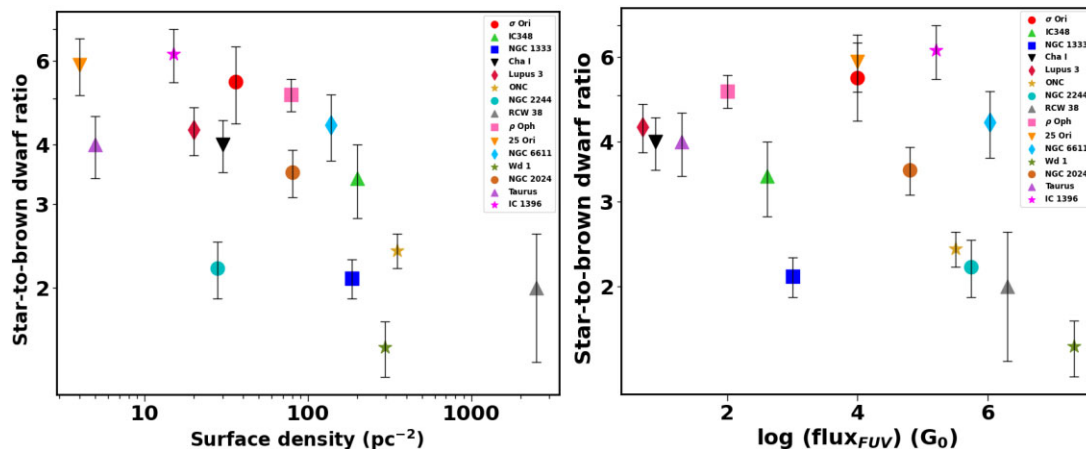


Figure 9. Variation of star-to-BD ratio versus (left) stellar surface density and (right) incident FUV flux.

5.2.1 Impact of stellar density

According to theoretical simulations, dynamical interactions among the self-gravitating cores in isolated parts of dense molecular clouds or inside filaments and circumstellar discs may lead to the subsequent ejection of stellar embryos (Bonnell et al. 2008; Whitworth 2018). Such low-mass collapsing cores, depleted of the material reservoir required for accretion eventually form substellar objects (Bonnell et al. 2008; Stamatellos & Whitworth 2009; Chabrier et al. 2014; Vorobyov et al. 2017; Riaz et al. 2018; Whitworth 2018). External factors like stellar density may play a crucial role in the pre-mature ejection of substellar cores. For example, close dynamical encounters with nearby stars are a common phenomenon in cluster environments with high stellar density. Such gravitational encounters can enhance the dynamical interactions among the isolated fragments or introduce perturbations in the star-disc system (Winter et al. 2018) thus, leading to the early ejection of stellar embryos (Bonnell et al. 2008; Stamatellos & Whitworth 2009; Portegies Zwart 2016; Vorobyov et al. 2017). Bonnell et al. (2008) find that the fraction of BDs in a region becomes twice as the stellar density enhances by an order of magnitude. The authors hence hypothesize that high density favours BD formation. Similarly Vorobyov et al. (2017) conclude that prograde close encounter can result into early ejection of fragments of BD mass regime. Riaz et al. (2018) also find a moderate impact of density perturbations on the formation of BDs and very low mass stars. In the recent studies by Mužić et al. (2017, 2019), the authors perform observational analysis of RCW 38 and NGC 2244, the two cluster environments with remarkably contrasting stellar densities, but are inconclusive about any variation in the BD formation efficiency with respect to either stellar density or presence of OB stars. The most recent study by Almendros-Abad et al. (2023) also supports this result and does not find any dependence of the star-to-BD ratio on the stellar density. However, these studies lack a comprehensive analysis for a miscellany of star-forming regions and are restricted to inner regions of the respective clusters.

We check the variation of star-to-BD ratio with respect to stellar density across 15 star-forming regions in Fig. 9 (left). The error bars on each point denote the uncertainty in star-to-BD ratio for the respective star-forming region. We observe that the star-to-BD ratio tends towards lower values at high stellar densities which, agrees with the theoretical hypothesis that high stellar densities favour the formation of BDs (Bonnell et al. 2008). This behaviour is however, more conspicuous at stellar densities > 50 stars pc^{-2} , which suggests

that stellar densities ought to be sufficiently high so as to promote dynamical encounters and effectuate the ejection of substellar cores. We also calculate the correlation coefficient to support our results. Since from Fig. 9 (left), the star-to-BD ratio and stellar density appear to be monotonically related, we evaluate the Spearman's rank correlation coefficient (ρ). We find the coefficient ρ , to be ~ -0.7 which indicates a strong correlation between the two variables, with a statistical significance of 0.5 per cent which emphasizes the relation to be monotonic as well (Spearman 1987). We hereby conclude that the BD formation efficiency may get impacted by high stellar densities (> 50 stars pc^{-2}) but do not quantify these results as it is beyond the scope of this study.

5.2.2 Impact of FUV flux

Photo-erosion of self-gravitating cores in the vicinity of massive OB-stars is another mechanism of formation of BDs. The incident FUV and EUV radiation from the surrounding massive stars ionizes and erodes the infalling material before it can accrete onto the central core, thus resulting in the formation of a substellar object (Whitworth & Zinnecker 2004). However, whether this is a dominant formation mechanism or not is still ambiguous. For example, the recent study by Almendros-Abad et al. (2023) does not find any direct dependence of the BD formation on OB-stars but, observes BDs to be located in close proximity to OB stars in NGC 2244. The study is thus, inconclusive regarding the role of OB-stars on BD formation. In our present study, we try to explore the variation of star-to-BD ratio relative to the presence of massive stars. We use the compiled list in Table 2 to plot the variation of star-to-BD ratio R with the incident FUV flux in Fig. 9 (right), along with the respective error bars representing error in star-to-BD ratio for various star-forming regions.

Looking at Fig. 9 (right), we are unable to make out a distinct correlation between the incident flux and star-to-BD ratio. The ratio however, appears to decline with increasing flux at $\log(\text{flux}_{\text{FUV}}) > 4 G_0$. This could likely be the effect of photo-erosion at high UV-fluxes or high stellar density observed in these regions since both the factors, that is high stellar density and high incident UV flux cannot be decoupled in massive star clusters. We are hence inconclusive regarding the effect of the presence of OB stars on BD formation efficiency. This result is also supported by Mužić et al. (2019) and Almendros-Abad et al. (2023), who do not find any clear dependence of BD fraction on the presence of OB stars based on the comparison among seven star-forming regions. This suggests that photo-erosion

Table 3. BDs within the central 22 arcmin radius region identified in this study. The columns present the RA, Dec., photometry, and the respective errors in r_2 , i_2 , and Y filters and the mass of these sources.

RA (deg)	Dec. (deg)	r_2 (mag)	$r_{2\text{err}}$ (mag)	i_2 (mag)	$i_{2\text{err}}$ (mag)	Y (mag)	Y_{err} (mag)	Mass (M_{\odot})
325.0996	57.7831	23.74	0.01	20.61	0.00	18.34	0.00	0.07
325.2094	57.7277	24.22	0.01	20.30	0.00	18.57	0.00	0.06
324.7828	57.4264	24.07	0.01	20.56	0.00	18.91	0.00	0.06
324.0923	57.4959	23.85	0.01	20.54	0.00	18.78	0.00	0.06
324.4811	57.4484	23.69	0.01	20.11	0.00	18.40	0.00	0.06
324.4575	57.4969	26.06	0.06	21.49	0.00	19.65	0.00	0.04
324.3343	57.7497	25.55	0.03	21.08	0.00	19.01	0.00	0.03
324.1520	57.5092	24.45	0.02	20.98	0.00	19.29	0.00	0.06
324.1435	57.5154	24.92	0.03	21.04	0.00	19.30	0.00	0.06
325.1902	57.5676	24.23	0.01	20.86	0.00	19.17	0.00	0.06
324.4685	57.3126	22.74	0.00	20.11	0.00	18.40	0.00	0.07
324.3183	57.5488	22.72	0.00	19.96	0.00	18.33	0.00	0.07
324.1370	57.5015	23.51	0.01	20.74	0.00	19.22	0.00	0.06
324.2120	57.6214	22.73	0.00	20.01	0.00	18.50	0.00	0.07
325.3353	57.3186	22.79	0.00	20.24	0.00	18.70	0.00	0.07
325.3433	57.3237	22.85	0.00	20.31	0.00	18.76	0.00	0.07
325.1490	57.2933	22.50	0.00	20.03	0.00	18.64	0.00	0.07
325.1416	57.3540	23.36	0.00	20.63	0.00	19.06	0.00	0.06
324.9703	57.4901	22.66	0.00	19.86	0.00	18.29	0.00	0.07
325.0021	57.5585	22.83	0.00	20.22	0.00	18.69	0.00	0.07
325.1468	57.6155	22.80	0.00	20.27	0.00	18.65	0.00	0.07
324.9589	57.3731	23.33	0.01	20.57	0.00	18.78	0.00	0.07
324.9279	57.4383	22.71	0.00	20.09	0.00	18.38	0.00	0.07
324.9290	57.4600	23.03	0.00	20.42	0.00	18.69	0.00	0.07
324.9169	57.5325	23.47	0.01	20.75	0.00	18.98	0.00	0.06
324.5742	57.2674	23.91	0.01	21.04	0.00	19.34	0.00	0.06
324.3852	57.4135	24.95	0.02	21.79	0.00	19.66	0.00	0.06
324.4519	57.4703	23.22	0.01	20.14	0.00	18.74	0.00	0.07
324.4618	57.4889	23.83	0.01	20.57	0.00	18.60	0.00	0.06
324.5109	57.4804	24.43	0.02	20.87	0.00	19.16	0.00	0.06
324.5797	57.5147	23.87	0.01	20.88	0.00	19.30	0.00	0.06
324.4841	57.5443	23.76	0.01	20.54	0.00	18.70	0.00	0.06
324.1735	57.5382	23.53	0.01	20.54	0.00	18.32	0.00	0.06
324.2134	57.5346	24.34	0.01	20.91	0.00	19.15	0.00	0.06
324.1619	57.5102	25.72	0.06	21.93	0.00	19.89	0.00	0.06
324.1149	57.6079	24.68	0.02	21.06	0.00	19.43	0.00	0.06
324.9834	57.2734	23.68	0.01	20.78	0.00	18.97	0.00	0.06
325.2606	57.3339	23.23	0.01	20.25	0.00	18.51	0.00	0.07
325.1878	57.4292	24.15	0.01	21.15	0.00	19.25	0.00	0.06
325.0855	57.3392	24.07	0.01	21.01	0.00	19.30	0.00	0.06
325.0216	57.5352	24.29	0.01	20.83	0.00	19.29	0.00	0.06
325.0511	57.6162	23.92	0.01	20.96	0.00	19.13	0.00	0.06
325.1674	57.6198	24.99	0.02	21.74	0.00	19.95	0.00	0.06
325.1083	57.7926	23.97	0.01	21.03	0.00	18.95	0.00	0.06
325.0825	57.7862	26.36	0.06	22.62	0.00	20.49	0.00	0.05
324.7593	57.1508	23.92	0.01	20.67	0.01	18.82	0.00	0.06
324.8858	57.2525	22.92	0.00	20.08	0.00	18.42	0.00	0.07
324.9626	57.4817	23.20	0.01	20.32	0.00	18.49	0.00	0.07
324.9151	57.5068	24.70	0.02	21.11	0.00	18.81	0.00	0.06
324.8126	57.5849	23.38	0.01	20.50	0.00	18.70	0.00	0.06
324.9211	57.6997	25.34	0.03	21.72	0.00	19.79	0.00	0.06
324.8863	57.7422	24.23	0.01	20.83	0.00	19.24	0.00	0.06
324.8643	57.2352	22.46	0.00	19.77	0.00	18.38	0.00	0.07
324.5316	57.5287	22.50	0.00	19.37	0.00	17.60	0.00	0.07
324.5085	57.6752	23.20	0.01	19.79	0.00	17.90	0.00	0.07
324.2213	57.5187	23.68	0.01	20.08	0.00	18.42	0.00	0.06
324.2461	57.4858	22.46	0.00	18.80	0.00	17.05	0.00	0.07
324.1375	57.4803	22.25	0.00	18.85	0.00	17.32	0.00	0.08
324.7057	57.4316	22.33	0.00	19.41	0.00	18.10	0.00	0.08
324.6640	57.6054	22.58	0.00	19.61	0.00	18.23	0.00	0.07
325.1605	57.4679	23.16	0.00	18.91	0.00	17.42	0.00	0.07
324.6305	57.4982	22.31	0.00	19.68	0.00	18.08	0.00	0.08

may not be the dominant mode of BD formation. However, more comprehensive substellar studies of massive clusters with rich OB-stars population like Cygnus OB2, NGC 3603, W3/W4/W5, Arches, and Quintuplet cluster, etc., are required to draw any conclusive results.

We caution the readers that although for the same mass range (0.03–1 M_{\odot}), our comparative analysis however covers different areas of study considered in the respective reference studies to calculate the ratio R in different star-forming regions. Another obvious caveat in such comparisons with literature values is the method by which the masses are estimated in each study. We do not consider the mass segregation effect or variation in spatial distribution of BDs as it is beyond the scope of this study.

6 SUMMARY AND FUTURE WORKS

BDs form the bridge between stars and planets and hence, it is crucial to study the nature of mass distribution down to substellar regime. The effect of cluster environment on the BD formation efficiency is another crucial aspect which still requires comprehensive studies, both theoretical and observational. We study the central 22 arcmin radius region of IC 1396, a nearby (< 1 kpc) prominent H II region with feedback driven cluster environment ideal for our study.

(1) We observed two pointings each of 1.5° diameter centred at IC 1396 with *Subaru* HSC in r_2 , i_2 , and Y filters. We however perform a deep analysis of the central 22 arcmin radius region as it covers ~ 60 per cent of the previously identified sources. This is the deepest study of this region as of yet with detected sources reaching down to $r_2 \sim 28$ mag.

(2) We perform a multiwavelength study of the region using *Subaru* HSC, *Gaia*, Pan-STARRS, and UKIDSS/2MASS data and obtain the candidate members using ML tools such as GMM and RF classifier. We then perform SED fitting of the probable members using VOSA tool. We also define the PMS locus and include sources within 1σ as members. Eventually we obtain 458 good quality sources along with their stellar parameters as cluster members.

(3) Among these members we identify 62 sources as BDs with mass $\leq 0.08 M_{\odot}$ and obtain the mass distribution down to substellar regime for a mass range 0.03–1 M_{\odot} . The star-to-BD ratio R turns out to be $\sim 6.0 \pm 0.8$ which is compatible with the range found for other star-forming regions for the same mass range.

(4) We find that within IC 1396, the BD fraction increases with increasing radial distance from the central massive star HD 206267. The O-stars present in IC 1396 influence the star-to-BD ratio across the region.

(5) We perform a comprehensive analysis of 15 star-forming regions to test the influence of environmental factors like stellar density (~ 4 –2500 stars pc^{-2}) and incident FUV flux (~ 0.7 –7.3 G_0), on the star-to-BD ratio. We conclude that BD formation efficiency may be affected by high stellar densities, but the effect of the incident FUV flux within this range is unclear.

As the next step, we aim to perform a similar analysis for the entire observed region of IC 1396 and obtain the substellar mass distribution for the complex. We also plan to identify the young stellar objects in the region and perform a circumstellar disc analysis to understand the variation of disc fraction with external factors like stellar density and incident FUV flux across the cluster.

ACKNOWLEDGEMENTS

The authors thank the referee for the useful constructive comments which has refined the overall structure, quality and comprehensibility

of this paper. This research is based on data collected at *Subaru* Telescope with Hyper Suprime-Cam, which is operated by the National Astronomical Observatory of Japan. We are honoured and grateful for the opportunity of observing the Universe from Mauna Kea, which has the cultural, historical, and natural significance in Hawaii. We are grateful to The East Asian Observatory which is supported by The National Astronomical Observatory of Japan; Academia Sinica Institute of Astronomy and Astrophysics; the Korea Astronomy and Space Science Institute; the Operation, Maintenance and Upgrading Fund for Astronomical Telescopes and Facility Instruments, budgeted from the Ministry of Finance (MOF) of China and administrated by the Chinese Academy of Sciences (CAS), as well as the National Key R&D Program of China (no. 2017YFA0402700). We use Pan-STARRS and *Gaia* DR3 data for the membership analysis in this work. The Pan-STARRS1 Surveys (PS1) and the PS1 public science archive have been made possible through contributions by the Institute for Astronomy, the University of Hawaii, the Pan-STARRS Project Office, the Max-Planck Society and its participating institutes, the Max Planck Institute for Astronomy, Heidelberg and the Max Planck Institute for Extraterrestrial Physics, Garching, The Johns Hopkins University, Durham University, the University of Edinburgh, the Queen's University Belfast, the Harvard-Smithsonian Center for Astrophysics, the Las Cumbres Observatory Global Telescope Network Incorporated, the National Central University of Taiwan, the Space Telescope Science Institute, the National Aeronautics and Space Administration under grant no. NNX08AR22G issued through the Planetary Science Division of the NASA Science Mission Directorate, the National Science Foundation grant no. AST-1238877, the University of Maryland, Eotvos Lorand University (ELTE), the Los Alamos National Laboratory, and the Gordon and Betty Moore Foundation. This work has made use of data from the European Space Agency (ESA) mission *Gaia* processed by Gaia Data processing and Analysis Consortium (DPAC: <https://www.cosmos.esa.int/web/gaia/dpac/consortium>). This publication makes use of VOSA, developed under the Spanish Virtual Observatory (<https://svo.cab.inta-csic.es>) project funded by MCIN/AEI/10.13039/501100011033/ through grant PID2020-112949GB-I00. VOSA has been partially updated by using funding from the European Union's Horizon 2020 Research and Innovation Programme, under grant agreement no. 776403 (EXOPLANETS-A). We gratefully acknowledge the use of high performance computing facilities at IUCAA, Pune for the HSC data reduction.

The authors thank Kora Mužić for the valuable review and suggestions which have improved the quality of the paper overall, Surhud More for his help during HSC data reduction. We thank Gregory J. Herczeg for his valuable help with the observing proposal for *Subaru* HSC for IC 1396 observations. We thank Isabelle Baraffe for providing us with isochrone models for an interval of $\log(\text{Age}) = 0.01$, through personal communication. JJ acknowledges the financial support received through the DST-SERB grant SPG/2021/003850. SRD acknowledges support from FONDECYT Postdoctoral fellowship (project code: 3220162). ZG is supported by the ANID FONDECYT Postdoctoral program no. 3220029. ZG acknowledge support by ANID – Millennium Science Initiative Program – NCN19_171.

7 DATA AVAILABILITY

Table 3 presents the optical HSC photometry along with the mass of the BDs identified in this study. The complete catalogue of

the identified members underlying this article will be shared on reasonable request to the corresponding author.

REFERENCES

- Aihara H. et al., 2018, *PASJ*, 70, S8
- Allard F., Homeier D., Freytag B., 2012, *Phil. Trans. R. Soc. Lond. Ser. A*, 370, 2765
- Allers K. N., Liu M. C., 2020, *PASP*, 132, 104401
- Almendros-Abad V. et al., 2023, *A&A*, 677, A26
- Alves de Oliveira C., Moraux E., Bouvier J., Bouy H., 2012, *A&A*, 539, A151
- Alves de Oliveira C., Moraux E., Bouvier J., Duchêne G., Bouy H., Maschberger T., Hudelot P., 2013, *A&A*, 549, A123
- Andersen M., Meyer M. R., Robberto M., Bergeron L. E., Reid N., 2011, *A&A*, 534, A10
- Andersen M., Gennaro M., Brandner W., Stolte A., de Marchi G., Meyer M. R., Zinnecker H., 2017, *A&A*, 602, A22
- Bailer-Jones C. A. L., Rybizki J., Fousneau M., Demleitner M., Andrae R., 2021, *AJ*, 161, 147
- Baraffe I., Homeier D., Allard F., Chabrier G., 2015, *A&A*, 577, A42
- Barentsen G. et al., 2011, *MNRAS*, 415, 103
- Bastian N., Covey K. R., Meyer M. R., 2010, *ARA&A*, 48, 339
- Bate M. R., 2012, *MNRAS*, 419, 3115
- Bayo A., Rodrigo C., Barrado Y Navascués D., Solano E., Gutiérrez R., Morales-Calderón M., Allard F., 2008, *A&A*, 492, 277
- Béjar V. J. S., Zapatero Osorio M. R., Rebolo R., Caballero J. A., Barrado D., Martín E. L., Mundt R., Bailer-Jones C. A. L., 2011, *ApJ*, 743, 64
- Bonnell I. A., Clark P., Bate M. R., 2008, *MNRAS*, 389, 1556
- Bosch J. et al., 2018, *PASJ*, 70, S5
- Briceño C., Hartmann L., Hernández J., Calvet N., Vivas A. K., Furesz G., Szentgyorgyi A., 2007, *ApJ*, 661, 1119
- Burgasser A. et al., 2019, *BAAS*, 51, 547
- Cantat-Gaudin T. et al., 2018, *A&A*, 618, A93
- Cantat-Gaudin T. et al., 2019, *A&A*, 624, A126
- Chabrier G., Johansen A., Janson M., Rafikov R., 2014, in Beuther H., Klessen R. S., Dullemond C. P., Henning T.eds, *Protostars and Planets VI*. University of Arizona Press, Tucson, AZ, p. 619
- Chambers K. C. et al., 2016, preprint (arXiv:1612.05560)
- Contreras M. E., Sicilia-Aguilar A., Muzerolle J., Calvet N., Berlind P., Hartmann L., 2002, *AJ*, 124, 1585
- Cutri R. M. et al., 2003, 2MASS All Sky Catalog of point sources
- Damian B., Jose J., Samal M. R., Moraux E., Das S. R., Patra S., 2021, *MNRAS*, 504, 2557
- Damian B., Jose J., Biller B., Paul K. T., 2023a, *J. Astrophys. Astron.*, 44, 77
- Damian B. et al., 2023b, *ApJ*, 951, 139
- Damiani F., Prisinzano L., Pillitteri I., Micela G., Sciortino S., 2019, *A&A*, 623, A112
- Das S. R., Gupta S., Prakash P., Samal M., Jose J., 2023, *ApJ*, 948, 7
- Downes J. J. et al., 2014, *MNRAS*, 444, 1793
- Drass H., Haas M., Chini R., Bayo A., Hackstein M., Hoffmeister V., Godoy N., Vogt N., 2016, *MNRAS*, 461, 1734
- Errmann R. et al., 2013, *Astron. Nachr.*, 334, 673
- Esplin T. L., Luhman K. L., 2017, *AJ*, 154, 134
- Esplin T. L., Luhman K. L., 2019, *AJ*, 158, 54
- Fujii M. S., Portegies Zwart S., 2016, *ApJ*, 817, 4
- Gaia Collaboration, 2021, *A&A*, 649, A1
- Gaia Collaboration, 2023, *A&A*, 674, A1
- Galli P. A. B. et al., 2020, *A&A*, 643, A148
- Gao X.-H., 2018a, *Ap&SS*, 363, 232
- Gao X., 2018b, *ApJ*, 869, 9
- Gao X.-h., 2019, *PASP*, 131, 044101
- Gennaro M. et al., 2018, *ApJ*, 855, 20
- Getman K. V., Feigelson E. D., Garmire G., Broos P., Wang J., 2007, *ApJ*, 654, 316
- Getman K. V., Feigelson E. D., Sicilia-Aguilar A., Broos P. S., Kuhn M. A., Garmire G. P., 2012, *MNRAS*, 426, 2917
- Guarcello M. G. et al., 2016, preprint (arXiv:1605.01773)
- Guarcello M. G. et al., 2021, *A&A*, 650, A157
- Gupta S. et al., 2021, *MNRAS*, 508, 3388
- Guzmán-Díaz J. et al., 2021, *A&A*, 650, A182
- Hewett P. C., Warren S. J., Leggett S. K., Hodgkin S. T., 2006, *MNRAS*, 367, 454
- Huston M. J., Luhman K. L., 2021, *AJ*, 161, 138
- Jose J., Herczeg G. J., Samal M. R., Fang Q., Panwar N., 2017, *ApJ*, 836, 98
- Jose J. et al., 2020, *ApJ*, 892, 122
- Kawanomoto S. et al., 2018, *PASJ*, 70, 66
- Kim J. S., Hartman P., Haworth Thomas J., Fang M., Facchini S., Pascucci I., Heo J.-E., 31st Jan 2022, in *Cambridge Workshop on Cool Stars, Stellar Systems, and the Sun*. Cambridge Workshop on Cool Stars, Stellar Systems, and the Sun. p. 196
- Kirkpatrick J. D. et al., 2012, *ApJ*, 753, 156
- Kirkpatrick J. D. et al., 2021, *ApJS*, 253, 7
- Kirkpatrick J. D. et al., 2023, preprint (arXiv:2312.03639)
- Knight C., Peeters E., Wolfire M., Stock D. J., 2022, *MNRAS*, 510, 4888
- Kroupa P., Boily C. M., 2002, *MNRAS*, 336, 1188
- Ksoll V. F. et al., 2021, *AJ*, 161, 257
- Kubiak K., Mužić K., Sousa I., Almendros-Abad V., Köhler R., Scholz A., 2021, *A&A*, 650, A48
- Lawrence A. et al., 2007, *MNRAS*, 379, 1599
- Levine J. L., Steinhauer A., Elston R. J., Lada E. A., 2006, *ApJ*, 646, 1215
- Lim B., Chun M.-Y., Sung H., Park B.-G., Lee J.-J., Sohn S. T., Hur H., Bessell M. S., 2013, *AJ*, 145, 46
- Lim B., Sung H., Hur H., Park B.-G., 2015, preprint (arXiv:1511.01118)
- Lindgren L. et al., 2021, *A&A*, 649, A2
- Longmore S. N. et al., 2014, in Beuther H., Klessen R. S., Dullemond C. P., Henning T.eds, *Protostars and Planets VI*. University of Arizona Press, Tucson, AZ, p. 291
- Lu J. Y., Liu Z. Q., Kabin K., Jing H., Zhao M. X., Wang Y., 2013, *J. Geophys. Res. (Space Phys.)*, 118, 3113
- Lucas P. W. et al., 2008, *MNRAS*, 391, 136
- Luhman K. L., Hapich C. J., 2020, *AJ*, 160, 57
- Luhman K. L., Herrmann K. A., Mamajek E. E., Esplin T. L., Pecaut M. J., 2018, *AJ*, 156, 76
- Marton G. et al., 2023, *A&A*, 674, A21
- Mejías A., Minniti D., Alonso-García J., Beamín J. C., Saito R. K., Solano E., 2022, *A&A*, 660, A131
- Melton E., 2020, *AJ*, 159, 200
- Mercer E. P., Miller J. M., Calvet N., Hartmann L., Hernandez J., Sicilia-Aguilar A., Gutermuth R., 2009, *AJ*, 138, 7
- Miret-Roig N. et al., 2019, *A&A*, 631, A57
- Miret-Roig N., Galli P. A. B., Olivares J., Bouy H., Alves J., Barrado D., 2022, *A&A*, 667, A163
- Morales-Calderón M. et al., 2009, *ApJ*, 702, 1507
- Mužić K., Scholz A., Geers V., Jayawardhana R., Tamura M., 2012, *ApJ*, 744, 134
- Mužić K., Schödel R., Scholz A., Geers V. C., Jayawardhana R., Ascenso J., Cieza L. A., 2017, *MNRAS*, 471, 3699
- Mužić K., Scholz A., Peña Ramírez K., Jayawardhana R., Schödel R., Geers V. C., Cieza L. A., Bayo A., 2019, *ApJ*, 881, 79
- Mužić K., Almendros-Abad V., Bouy H., Kubiak K., Peña Ramírez K., Krone-Martins A., Moitinho A., Conceição M., 2022, *A&A*, 668, A19
- Mužić K., Scholz A., Geers V. C., Jayawardhana R., 2015, *ApJ*, 810, 159
- Nakano M., Sugitani K., Watanabe M., Fukuda N., Ishihara D., Ueno M., 2012, *AJ*, 143, 61
- Offner S. S. R., Clark P. C., Hennebelle P., Bastian N., Bate M. R., Hopkins P. F., Moraux E., Whitworth A. P., 2014, in Beuther H., Klessen R. S., Dullemond C. P., Henning T.eds, *Protostars and Planets VI*. University of Arizona Press, Tucson, AZ, p. 53
- Okada Y., Onaka T., Nakagawa T., Shibai H., Tomono D., Yui Y. Y., 2006, *ApJ*, 640, 383

- Olivares J. et al., 2019, *A&A*, 625, A115
- Oliveira J. M., Jeffries R. D., van Loon J. T., 2009, *MNRAS*, 392, 1034
- Olsen C. et al., 2021, *ApJ*, 913, 45
- Patel N. A., Goldsmith P. F., Heyer M. H., Snell R. L., Pratap P., 1998, *ApJ*, 507, 241
- Peña Ramírez K., Béjar V. J. S., Zapatero Osorio M. R., Petr-Gotzens M. G., Martín E. L., 2012, *ApJ*, 754, 30
- Pearson S., Scholz A., Teixeira P. S., Mužić K., Almendros-Abad V., 2021, *MNRAS*, 507, 4074
- Pedregosa F. et al., 2011, *J. Mach. Learn. Res.*, 12, 2825
- Pelayo-Baldarrago M. E., Sicilia-Aguilar A., Fang M., Roccatagliata V., Kim J. S., García-Álvarez D., 2023, *A&A*, 669, A22
- Portegies Zwart S. F., 2016, *MNRAS*, 457, 313
- Portegies Zwart S. F., McMillan S. L. W., Gieles M., 2010, *ARA&A*, 48, 431
- Povich M. S., Maldonado J. T., Nuñez E. H., Robitaille T. P., 2019, *ApJ*, 881, 37
- Prisinzano L. et al., 2022, *A&A*, 664, A175
- Reipurth B., Clarke C., 2001, *AJ*, 122, 432
- Riaz R., Vanaverbeke S., Schleicher D. R. G., 2018, *MNRAS*, 478, 5460
- Robberto M. et al., 2020, *ApJ*, 896, 79
- Sarro L. M. et al., 2014, *A&A*, 563, A45
- Saurin T. A., Bica E., Bonatto C., 2012, *MNRAS*, 421, 3206
- Scholz A., Muzic K., Geers V., Bonavita M., Jayawardhana R., Tamura M., 2012, *ApJ*, 744, 6
- Scholz A., Geers V., Clark P., Jayawardhana R., Muzic K., 2013, *ApJ*, 775, 138
- Sicilia-Aguilar A., Hartmann L. W., Briceño C., Muzerolle J., Calvet N., 2004, *AJ*, 128, 805
- Sicilia-Aguilar A., Hartmann L. W., Hernández J., Briceño C., Calvet N., 2005, *AJ*, 130, 188
- Sicilia-Aguilar A. et al., 2006, *ApJ*, 638, 897
- Sicilia-Aguilar A., Kim J. S., Sobolev A., Getman K., Henning T., Fang M., 2013, *A&A*, 559, A3
- Sicilia-Aguilar A., Roccatagliata V., Getman K., Henning T., Merín B., Eiroa C., Rivière-Marichalar P., Currie T., 2014, *A&A*, 562, A131
- Sicilia-Aguilar A., Patel N., Fang M., Roccatagliata V., Getman K., Goldsmith P., 2019, *A&A*, 622, A118
- Silverberg S. M., Günther H. M., Kim J. S., Principe D. A., Wolk S. J., 2021, *AJ*, 162, 279
- Slesnick C. L., Hillenbrand L. A., Carpenter J. M., 2004, *ApJ*, 610, 1045
- Spearman C., 1987, *Am. J. Psychol.*, 100, 441
- Stamatellos D., 2014, in *The Labyrinth of Star Formation*. Springer International Publishing, Switzerland, p. 17 The
- Stamatellos D., Whitworth A. P., 2009, *MNRAS*, 392, 413
- Suárez G., Downes J. J., Román-Zúñiga C., Cerviño M., Briceño C., Petr-Gotzens M. G., Vivas K., 2019, *MNRAS*, 486, 1718
- Vorobyov E. I., Basu S., 2013, *Mem. Soc. Astron. Ital.*, 84, 866
- Vorobyov E. I., Steinrueck M. E., Elbakyan V., Guedel M., 2017, *A&A*, 608, A107
- Wang S., Chen X., 2019, *ApJ*, 877, 116
- Whitworth A., 2018, preprint (arXiv:1811.06833)
- Whitworth A. P., Zinnecker H., 2004, *A&A*, 427, 299
- Winston E., Wolk S. J., Bourke T. L., Megeath S. T., Gutermuth R., Spitzbart B., 2011, *ApJ*, 743, 166
- Winston E., Hora J. L., Tolls V., 2020, *AJ*, 160, 68
- Winter A., 2019, PhD thesis. University of Cambridge, UK
- Winter A. J., Haworth T. J., 2022, *Eur. Phys. J. Plus*, 137, 1132
- Winter A. J., Clarke C. J., Rosotti G., Ih J., Facchini S., Haworth T. J., 2018, *MNRAS*, 478, 2700
- Zapatero Osorio M. R., Béjar V. J. S., Peña Ramírez K., 2017, *ApJ*, 842, 65
- de Zeeuw P. T., Hoogerwerf R., de Bruijne J. H. J., Brown A. G. A., Blaauw A., 1999, *AJ*, 117, 354

APPENDIX A: DATA QUALITY COMPARISON

In this section, we present two data quality plots of the HSC data used in this study. As can be seen from Fig. A1 (top), the completeness of

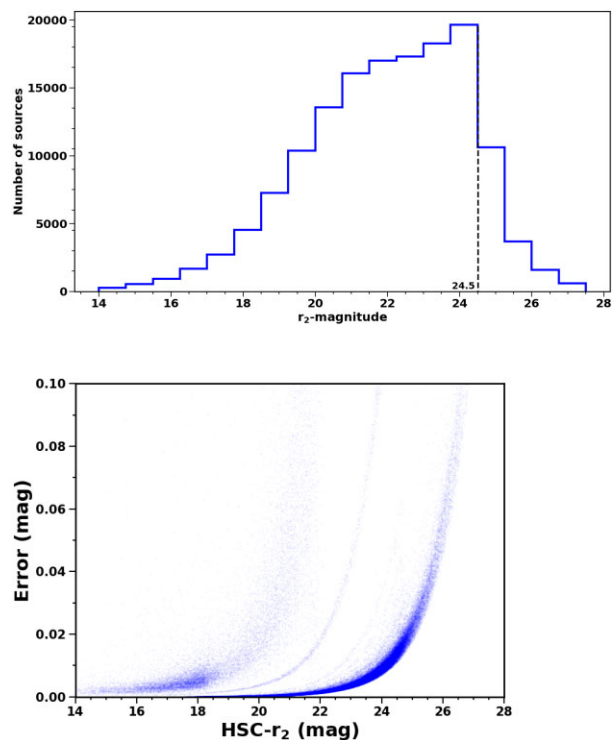


Figure A1. Top: completeness of HSC r_2 filter based on the peak (turnover point) of distribution (Jose et al. 2017; Gupta et al. 2021). Bottom: error versus magnitude for r_2 filter. The three branches observed in the HSC r_2 -band plot correspond to the merged Pan-STARRS photometry, and long and short exposure photometry.

the data in r_2 band is down to 24.5 mag ($\sim 0.03 M_{\odot}$). The majority of sources have photometric error ≤ 0.05 mag as evident from Fig. A1 (bottom). The three branches observed in the HSC r_2 -band plot correspond to the merged Pan-STARRS photometry (used while generating the deep optical catalogue as mentioned in Section 2.2), long and short exposure photometry. More details about merging of the short and long exposure catalogues will be presented in Das et al. (in preparation). We compare the proper motion and parallax distribution of *Gaia* DR3 counterparts of the members identified in this study with that of the previous studies. Figs A2 (top and bottom) suggest an excellent concordance between the proper motion and distance estimates of the new and literature-based cluster members. Also, we observe an unavoidable yet limited scatter in the proper motions and distance values of the members identified in this study as compared to the literature-based members. However, some scatter is inevitable in all membership analysis and has been observed in previous studies (Cantat-Gaudin et al. 2018; Pelayo-Baldarrago et al. 2023; Das et al. 2023) as well.

Hyperparameters for all the phases of RF classifier are as follows:

- random state = 50
- number of estimators = 188
- min_samples_split: 5
- max_leaf_nodes: 14
- max_features: 0.6
- max_depth: 16

We provide all the necessary details of the entire RF process like accuracy, precision, recall, F1 score, and CV score for each phase in Table A1. We have also included the ROC curves for the three phases here.

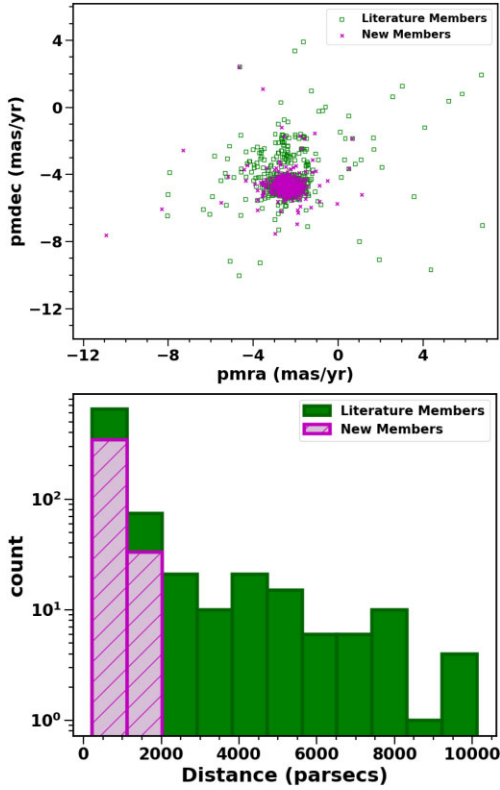


Figure A2. Top: proper motion RA versus Dec. distribution and bottom: distance distribution for cluster members identified by previous studies versus members from this study with *Gaia* DR3 counterparts. We observe a small scatter in the proper motions and distance values of the members identified in this study as compared to the literature-based members. However, some scatter is inevitable in all membership analysis.

APPENDIX B: FIELD SUBTRACTION METHOD FOR VALIDATION

We consider a 10 arcmin radius control field located towards the outskirts of the HSC observed area of IC 1396 and perform statistical field decontamination of the cluster field, located towards the centre of the same area. An area of only 10 arcmin radius is chosen here for field subtraction due to the lack of a suitable control field of larger area, devoid of young PMS stars, as observed by their spatial distribution (Das et al., in preparation). The 10 arcmin radius control field considered for the field subtraction here is chosen carefully towards the outskirts as it is devoid of any PMS sources which is suggested by the spatial density map given in Das et al. (2023). We perform the field decontamination by dividing the $r_2 - Y$ colour and r_2 magnitude parameter space into 0.1 mag bins, followed by the subtraction of the control field count from the cluster field count (Damian et al. 2021; Gupta et al. 2021). The member selection using PMS locus approach is then performed for the statistically subtracted sources located above the 10 Myr isochrone. Subsequently, sources within 1σ limit of the defined locus and $r_2 \geq 22$ mag are selected as members. However, we find that whether or not prior field subtraction is performed, the statistics of members as well as mass distribution remains approximately unaltered. We would like to emphasize here that the sources by field subtraction are not the actual cluster members but just the statistical members in the 10 arcmin central cluster field. Hence, we continue without field decontamination for PMS-based membership analysis as given in Section 3.4. This is because the cluster members obtained within 1σ of the empirical PMS locus are common in all the CMD combinations (as mentioned in Section 3.4). On the contrary, the candidate members selected from the field decontamination by statistical method need not be common across all combinations of different bands as they are not true members. Moreover, due to the lack of a suitable control field of 22 arcmin radius area, we are unable to perform decontamination for the central cluster considered for our analysis.

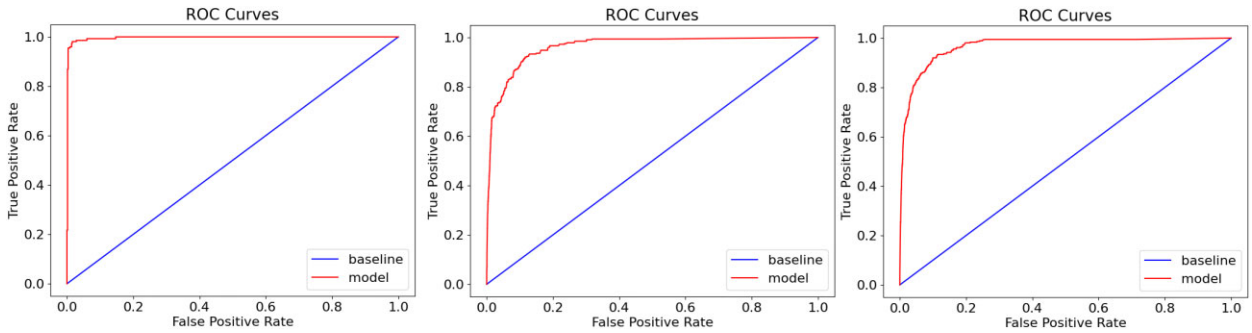


Figure A3. ROC curve for the (left) first RF classifier phase. Centre: second RF classifier phase. Right: third RF classifier phase.

Table A1. Quality parameters of the three RF classifier phases.

Phase	Accuracy	Precision	F1 score	Recall	CV score
Phase 1	0.98	0.98	0.95	0.93	0.98
Phase 2	0.98	0.80	0.70	0.60	0.98
Phase 3	0.98	0.72	0.70	0.62	0.98

This paper has been typeset from a $\text{\TeX}/\text{\LaTeX}$ file prepared by the author.